An atlas of neural crest lineages along the posterior developing zebrafish at single-cell resolution

Aubrey G.A. Howard IV[1], Phillip A. Baker[1], Rodrigo Ibarra-García-Padilla, Joshua A. Moore, Lucia J. Rivas, Eileen W. Singleton, Jessa L. Westheimer, Julia A. Corteguera, James J. Tallman, and Rosa A. Uribe*

Department of BioSciences, Rice University, 6100 Main Street, Houson, TX 77005, United States of America

***corresponding author**, *email address*: rosa.uribe@rice.edu

[1]These authors contributed equally to this work

Aubrey G.A. Howard IV contributed to conceptualization, data curation, formal analysis, methodology, investigation, validation, visualization, and writing – original draft preparation.

Phillip A. Baker contributed to conceptualization, data curation, formal analysis, methodology, investigation, validation, visualization, and writing – original draft preparation.

Rodrigo Ibarra-García-Padilla contributed to conceptualization, data curation, formal analysis, methodology, investigation, validation, visualization, and writing – original draft preparation.

Joshua A. Moore contributed to conceptualization, data curation, formal analysis, methodology, investigation, validation, visualization, and writing – original draft preparation.

Lucia J. Rivas contributed to investigation, validation, visualization, and writing – original draft preparation.

Eileen W. Singleton contributed to methodology, investigation, validation, and writing – review and editing.

Jessa L. Westheimer contributed to investigation, validation, visualization and writing – review and editing.

Julia A. Corteguera contributed to investigation, validation, visualization and writing – review and editing.

James J. Tallman contributed to validation, data curation and writing – review and editing

Rosa A. Uribe contributed to conceptualization, data curation, formal analysis, funding acquisition, investigation, methodology, project administration, resources, supervision, validation, visualization, and writing – original draft preparation.

Key words: neural crest, sox10, single-cell, zebrafish, neuron, pigment cell

ABSTRACT

Neural crest cells (NCCs) are vertebrate stem cells that give rise to various cell types throughout the developing body in early life. Here, we utilized single-cell transcriptomic analyses to delineate NCC-derivatives along the posterior developing vertebrate, zebrafish, during the late embryonic to early larval stage, a period when NCCs are actively differentiating into distinct cellular lineages. We identified several major NCC/NCC-derived cell-types including mesenchyme, neural crest, neural, neuronal, glial, and pigment, from which we resolved over three dozen cellular subtypes. We dissected gene expression signatures of pigment progenitors delineating into chromatophore lineages, mesenchyme subtypes, and enteric NCCs transforming into enteric neurons. Global analysis of NCC derivatives revealed they were demarcated by combinatorial *hox* gene codes, with distinct profiles within neuronal cells. From these analyses, we present a comprehensive cell-type atlas that can be utilized as a valuable resource for further mechanistic and evolutionary investigations of NCC differentiation.

INTRODUCTION

Unique to vertebrates, neural crest cells (NCCs) are an embryonic stem cell population characterized as transient, highly migratory, and multipotent. Following their birth from the dorsal neural tube, NCCs migrate extensively, dorsolaterally or ventrally along the main axial levels of the embryo; the cranial, vagal, trunk, and sacral regions (Graham et al., 2004; Le Douarin and Teillet et al., 1974). Depending on the axial level of their origination, NCCs give rise to cells within critical tissues, such as the cornea, craniofacial cartilage and bone, mesenchyme, pigment cells in the skin, as well as neurons and glia that comprise peripheral ganglia (Hutchins et al., 2018; Epstein et al., 1994; Kuo and Erickson, 2011; Hall and Hörstadius, 1988; Le Douarin and Kalcheim, 1999; Theveneau and Mayor, 2012; Williams and Bohnsack, 2015; Yntema and Hammond, 1954).

During their maturation, NCCs undergo dramatic transcriptional changes which lead to diverse cellular lineages, making their transcriptomic profiles highly dynamic (Simões-Costa et al., 2014; Martik et al., 2017; Soldatov et al., 2019; Williams et al., 2019). In support of the model that complex transcriptional programs govern NCC ontogenesis, the gene regulatory networks involved in development of NCCs to broad cell types has been described at a high level, especially during early NCC specification along cranial axial regions, across amniotes (Martik et al., 2017; Simoes-Costa and Bronner, 2016; Green et al. 2016; Williams et al., 2019). For example, *Sox10* encodes a conserved transcription factor that is expressed along all axial levels by early migrating NCCs and within their differentiating lineages (Sauka-Spengler and Bronner-Fraser, 2008; Martik et al., 2017). Despite this progress, however, comprehensive knowledge of the genes that participate in proper NCC development and their lineage differentiation programs during later phases of embryogenesis remains to be fully characterized, particularly for posterior tissues (reviewed in Hutchins et al., 2018). Indeed, improper regulation of NCC differentiation can cause several neurocristopathies, such as DiGeorge syndrome, neuroblastoma, Hirschsprung disease, Auriculo-condylar syndrome, and Klein-Waardenburg syndrome (Barlow, 1984; Bolande, 1997;

Brosens et al., 2016; Escot et al., 2016; Vega-Lopez et al., 2017; Wang et al., 2014), further highlighting the need to understand how NCCs differentiate into diverse cellular types.

While many studies have examined early phases of NCC specification, gene regulatory network construction, and NCC migration, we have extended analysis for the first time to characterize transcriptomic signatures of NCC-derived cells differentiating within posterior tissues of the zebrafish. Previous single-cell transcriptomic studies in zebrafish have laid a strong foundation to globally map early lineages of a majority of cell types through early to middle embryonic development (Wagner et al. 2018; Tambalo et al. 2020), and recently this has been extended into the larval stage (Farnsworth et al., 2019). With respect to the posterior NCC fates, however, many of these cells undergo differentiation programs during the embryonic to larval transition, a developmental stage that emerges between ~48 hpf to 72 hpf. Transcriptomic analysis during this transitional phase therefore would enhance our understanding of the dynamic shifts in cell states that may regulate cellular differentiation programs.

Beyond their strong advantages as a vertebrate embryonic model, zebrafish lend themselves to study transcriptomics. The rapid progression and thorough characterization of zebrafish embryonic development makes it possible to observe the onset of ontogenesis for most organs in a matter of hours to days, accelerating our ability to interrogate vertebrate development (Kimmel et al., 1995; Ahrens et al., 2013; Parichy et al., 2009). Zebrafish also share strong genetic conservation with other vertebrates (Howe et al., 2013), allowing for information gleaned to be easily translated to other model organisms or human studies (Bradford et al., 2017).

We have utilized the Tg(*-4.9sox10:EGFP*) (hereafter referred to as *sox10*:GFP) transgenic fish line to identify NCCs and their recent derivatives. As described by Carney et al., 2006, the *sox10*:GFP fish line allows for the labeling of NCCs, NCC-derived cells, and other ancillary tissues, such as the developing ear (otic) and select muscle cells, *in vivo*. Due to the widespread presence of *sox10* among NCCs (Carney et al., 2006), *sox10*:GFP functions as a useful marker

in zebrafish to identify cells fated to become major posterior cell lineages, including neurons, peripheral glia, mesenchyme, and pigment cells.

In this study, we have leveraged the power of single-cell transcriptomics and curated the identities of *sox10*-expressing and *sox10*-derived populations along the posterior zebrafish during development. Using *sox10*:GFP^{+} 48-50 hpf embryos and 68-70 hpf larvae, we identified eight major classes of cells: mesenchyme, neural crest, neural, neuronal, glial, pigment, muscle, and otic. Among the major cell types, we annotated over 40 cellular subtypes. We remarkably resolved the dynamic transition of several NCC fates, most notably we discovered over a dozen mesenchymal subtypes and captured the progressive differentiation of enteric neural progenitors into maturing enteric neurons. By computationally merging our 48-50 hpf and 68-70 hpf data sets, we generated a comprehensive atlas of *sox10*$^{+}$ cell types spanning the embryonic to larval transition, which can also be used as a tool to identify novel genes and mechanistically test their roles in the developmental progression of posterior NCCs. Additionally, using Hybridization Chain Reaction (HCR) and *in situ* hybridization, we validated the spatiotemporal expression patterns of various subtypes during the embryonic to larval transition. Lastly, we characterized a *hox* signature for each cell type, detecting novel combinatorial expression of *hox* genes within specific cell types. Our intention is that this careful analysis of posterior NCC fates and resulting Atlas will aid the cell and developmental biology communities by advancing our fundamental understanding of the diverging transcriptional landscape during the NCC's extensive cell fate acquisition.

RESULTS

Single-cell profiling of sox10:GFP^{+} cells along the posterior zebrafish during the embryonic and larval stage transition

To identify *sox10*-expressing and *sox10*-derived cells along the posterior zebrafish during the embryonic to larval transition, we utilized the transgenic line *sox10:*GFP (**Fig. 1A**) (Carney et al., 2006; Kwak et al., 2013). All tissue between the otic vesicle and hindgut, encompassing the entire vagal and trunk axial region (**Fig. 1B**), was dissected from 100 embryonic fish at 48-50 hours post fertilization (hpf) and 100 larval fishes at 68-70 hpf, thereby encompassing the embryonic to larval transition. Dissected tissues were dissociated and immediately subjected to fluorescence-activated cell sorting (FACS) to isolate *sox10*:GFP^{+} cells (**Fig. 1B**; **Fig. S1A,B**). To generate gene expression libraries for individual cells, isolated cells were then input into 10X Genomics Chromium scRNA-seq assays and captured at a depth of 2300 cells from the 48-50 hpf time point and 2580 cells from the 68-70 hpf time point (**Fig. 1C**; **Fig. S1C**). We performed cell filtering and clustering (**Fig. S1C-I**) of the scRNA-seq data sets using Seurat (Butler et al., 2018; Stuart et al., 2019) to computationally identify cell populations based on shared transcriptomes. Cells were filtered from this analysis, yielding 1608 cells from the 48-50 hpf time point and 2410 cells from the 68-70 hpf time point, totaling 4018 cells for final analysis (**Fig. S1C**). We detected cell population clusters with transcriptionally unique signatures, as shown in heatmap summaries that revealed the top 10 significant genes per cluster, with 19 clusters (0-18) from the 48-50 hpf time point (**Fig. 2A**) and 23 clusters (0-22) from the 68-70 hpf time point (**Fig. 3A**), totaling 42 clusters across both time points. The top significantly enriched markers for each cluster at 48-50 and 68-70 hpf are provided in **Table S1**.

Major classification of sox10:GFP^{+} cell types along the posterior developing body

Data sets were visualized with the t-Distributed Stochastic Neighbor Embedding (tSNE) method, which spatially grouped cells in each cluster to distinguish transcriptionally-distinct cell

populations, for both time points examined (**Fig. 2B, 3B**). To assess the general proliferative state of cells in each time point, we determined their G1, S or G2/M phase occupancy, based on expression of proliferative cell cycle marker genes (**Fig. S2I**). At 48-50 hpf, 52% of *sox10*:GFP^{+} cells were in G1 phase, while 31% were in the S phase and 17% in G2/M phase (**Fig. S2G**), collectively indicating that 48% of the cells in the 48-50 hpf time point were proliferative. At 68-70 hpf, 64% of cells were in G1 phase, while 24% of cells were in the S phase and 12% in G2/M phase (**Fig. S2G**), indicating that 36% of the cells were proliferative. The global cell cycle occupancy distributions of all of the cells were visualized in tSNE plots, thereby revealing congregations of proliferative and non-proliferative *sox10*:GFP^{+} cells (**Fig. S2A,B**). *aurkb* and *mcm3* confirmed general occupancy in the G2/M and S phase for each time point (**Fig. S2E-F**). Together, these data of cell cycle state reflect a general decrease in the number of proliferative cells among *sox10*:GFP^{+} populations along the posterior fish, in agreement with other observations of the proliferative state of *sox10*-derived cells in the embryo (Rajan et al., 2018).

To group cells into major tissue cell type categories, we performed curation analysis of the clustered data sets (**Fig. S3**; **Fig. 2,3**; **Fig. S2H**). Global analysis of scRNA-seq transcriptomes among cell clusters indicated that *sox10*:GFP^{+} cells exist in several major cell type categories in the embryo and larvae. These major cell type categories included: Neural, Neuronal, Glial, Mesenchyme, Pigment cell, Neural Crest, Otic, and Muscle (**Fig. S2H**; **Fig. 2C-F**; **Fig. 3C-F**). Neuronal clusters were identified by expression of the pan neuronal markers *elavl3*, *elavl4*, and/or *tuba2*, and encompassed Clusters 0, 7, and 17 at 48-50 hpf (19% of data set) and Clusters 5 and 12 at 68-70 hpf (10% of data set) (**Fig. S3**; **Fig. 2F**; **Fig. 3F**). Neural cell types were identified based on a combination of the neural markers *ncam1a/b, notch1a*, *dla*, *her4.1*, *ascl1a*, and/or *sox10* and included Cluster 13 at 48-50 hpf (4% of data set) and Clusters 3 and 10 at 68-70 hpf (13% of data set). Glial category cells consisted of Cluster 15 from 48-50 hpf (3% of data set) and Cluster 14 from 68-70 hpf (2% of data set), identified by the presence of the glial markers *plp1a*, *fabp7a, sox10, pou3f1, foxd3*, and/or *gfap* (**Fig. S3**; **Fig. 2F**; **Fig. 3F**). Cluster 8 at 48-50 hpf

exhibited expression of Pigment Cell development markers *tyrp1a/b*, *dct*, and *mitfa,* thereby encompassing 5% of the 48-50 hpf data set (**Fig. S3**; **Fig. 2F**). Subsequent Pigment Cell identity was detected in Clusters 4, 13, 15, 16, and 18 at 68-70 hpf (**Fig. S3**; **Fig. 3**), increasing to 14% of the data set (**Fig. S2H**), during which time the Pigment Cells diverged and expanded into distinct chromatophore lineages, as discussed further in **Fig. 4**. A Neural Crest cluster, Cluster 5 at 48-50 hpf (**Fig. 2**) (6% of data set), which we also discuss further in **Fig. 6**, was identified by the combined expression of *sox10*, *crestin*, *foxd3, ngfrb*, and *tfap2a*. Mesenchyme tissue identity among clusters represented the largest proportion of the data sets at 61% and 53% of the cells at 48-50 and 68-70 hpf, respectively (**Fig. S2H**). Mesenchyme clusters were identified by a combination of mesenchymal gene markers, including: *snai1a/b*, *twist1a/b*, *prrx1a/b*, *meox1*, *foxc1a/b*, *cdh11, sparc, colec12*, and/or *pdgfra*, as recently described in amniotes (Soldatov et al., 2019). Mesenchyme identity was detected in Clusters 1-4, 6, 9-12, and 14 at the 48-50 hpf time (**Fig. 2A-F**) and Clusters 0-2, 6-8, 17, 20, and 22 at the 68-70 hpf time point (**Fig. 3A-F**).

Our analysis also revealed the presence of other *sox10*-expressing cell types, as has previously been described in zebrafish (Carney et al., 2006; Rajan et al., 2018; Rodrigues et al., 2012; Kwak et al., 2013). We detected cells with an otic vesicle signature, via the markers *cldnb, vamp8, epcam*, or *otomp*, which were expressed in Clusters 16 at 48-50 hpf (1% of data set) (**Fig. 2C-F**; **Fig. S2H**; **Fig. S4**) and Cluster 11 at 68-70 hpf (3% of data set) (**Fig. 3C-F**). Cluster 18 at the 48-50 hpf time (1% of data set) and Clusters 9 and 19 at the 68-70 hpf time (5% of data set) displayed muscle gene expression via the markers *tpma, tnnc2, actc1b, ckmb* (**Fig. S3,S4**). Cluster 21 at 68-70 hpf (1% of data set) was not categorized (**Fig. S2H**), likely a spurious cell. Overall, major cell type cluster identities and top signature marker genes are summarized in a table (**Fig. S3**).

Posterior sox10:GFP^{+} cell subtype transcriptional signatures resolved

Analysis of each of the 42 cluster gene signatures among the two time points revealed distinct subpopulations of posterior *sox10*:GFP^{+} cells and their transcriptomes in the developing zebrafish. Notably, we identified previously described *sox10*-derived cell types. For example, we observed sensory neuronal gene expression in Cluster 17 at 48-50 hpf (**Fig. S3**, **Fig. S5**) by the markers *neurod1*, *neurod4, neurog1, six1a*/*b*, *elavl4*; markers known to be expressed in sensory cell progenitors and differentiating sensory neurons, such as in neural crest-derived dorsal root ganglion (DRG) in zebrafish during the 2nd day of development (Carney et al 2006; Delfino-Machín et al., 2017). The *sox10*:GFP line has been shown to transiently label DRG progenitors between the 1st and 2nd day of development (McGraw et al., 2008; Rajan et al., 2018). In addition, the scRNA-seq transcriptome data sets at both time points exhibited gene expression indicative of previously described neural crest-derived lineages (summarized in Hutchins et al., 2018) including mesenchymal cells (Le Lievre and Le Douarin, 1975; Kague et al., 2012; Soldatov et al., 2019; Ling and Sauka-Spengler, 2019), pigment cells (Reedy et al., 1998; Higdon et al., 2013), and enteric neurons (Kelsh and Eisen, 2000; Kuo and Erickson, 2011; Lasrado et al., 2017;), which we describe in further detail below and in Figures 4-7.

Pigment cell chromatophore lineages resolved

With robust genetic lineage details published on pigment cell differentiation in zebrafish (Kelsh, 2004; Lister, 2002; Quigley and Parichy, 2002), we sought to validate our scRNA-seq analysis pipeline by assessing if we could resolve pigment cell gene expression states. Pigment cell development has been broadly studied in the developing zebrafish, where neural crest cells give rise to three distinct chromatophore populations: melanophores, xanthophores, and iridophores (**Fig. 4A**). Melanophores are the first pigment cells to appear during embryonic zebrafish development, while xanthophores and iridophores differentiate later in the larvae (Kimmel et al., 1995). Melanophores, the best characterized population, express a combination of markers throughout their development including *mitfa*, *dct*, *tyrp1a/b*, and *pmela* (Du et al., 2003;

Lister et al., 1999; Ludwig et al., 2004; Quigley and Parichy, 2002). Similarly, the genes *pnp4a*, *tfec*, *gpnmb*, and *atic* are all enriched in iridophores and are critical for their maturation (Higdon et al., 2013; Lister et al., 2011; Petratou et al., 2018, 2019). Finally, differentiating xanthophores express *gch2*, *pax7a/b*, *xdh*, *mitfa*, and *aox5* (Nord et al., 2016; Parichy et al., 2000; Saunders et al., 2019; Minchin and Hughes, 2008; Lister et al., 1999).

Our cluster analysis of *sox10*:GFP^{+} single cell data sets revealed the robust presence of pigment cell lineages during the embryonic to larval transition (**Fig. 4B-J**; **Fig. S3**). At 48-50 hpf, melanophores were detected based on expression of the global pigment identity genes *mitfa*, *dct*, *tyrp1b*, and *pmela* (**Fig. 2F**; **Fig. 4A**). Of all the clusters identified at this time point, Cluster 8 presented significant levels of these genes, identifying it as a melanophore population (**Fig. 4B**). tSNE plots reveal that the melanophore markers indeed map strongly to Cluster 8 (**Fig. 4C**), which comprises the major cell type classified in the Pigment identity grouping (**Fig. 2D**).

At 68-70 hpf, we resolved discrete pigment cell populations that included xanthophore, iridophore, and two distinct melanophore clusters (**Fig. 4D-G**, **Fig. S3**). The xanthophores mapped to Cluster 15 (**Fig. S3**) and were enriched with *xdh*, *aox5*, *pax7b*, *mitfa*, and *gch2* (**Fig. 4D,F**). Cluster 16 we identified as iridophores, which presented the well characterized markers: *tfec*, *pnp4a*, *gpnmb*, and *atic* (**Fig. S3**; **Fig. 4A,D,G**). The use of cell cycle markers revealed that the two different melanophore clusters (Clusters 4 and 18) were present in different proliferative states. While the majority of cells in Cluster 4 were in G1, the presence of S and G2/M markers, such as *pcna* and *aurkb*, in melanophore Cluster 18 suggests that this population is proliferating melanophores (**Fig. S2B,E,F**; **Fig. S3E**; **TableS4**). While Clusters 4 and 18 shared a strong melanophore signature (**Fig. 4D**), they also expressed various other genes with previously known expression in pigment cells; such as *tfap2a*, *gch2*, *slc24a5*, and *gpr143* (Thisse et al., 2004). Overall, genes shared between Cluster 4 and Cluster 18, as well as their unique genes, are summarized in **Table S4**. Through the analysis of cell cycle markers, our observations regarding melanophore populations extend previous work performed in older mid-larval and juvenile stages,

where distinct differentiation and proliferative states between two melanophore clusters were described at 5 dpf (Saunders et al., 2019). Our detection of differing pigment proliferation states suggest that the two separate populations of melanophores appear during the early larval transition at 68-70 hpf. Indeed, we did not detect more than one subpopulation of melanophore based on proliferative state at 48-50 hpf, which were almost entirely in the G1 phase (**Fig. S2A,C,D**).

At 68-70 hpf, we were able to identify a pigment progenitor population, where iridophore and melanophore markers were co-expressed (**Fig. 4D,E,G**). Specifically, a bipotent irido-melano progenitor in which cells begin to acquire their final chromatophore fate has been described recently at 24, 30, and 48 hpf (Petratou et al. 2018), where these undifferentiated pigment progenitor cells express *tfec* in combination with *mitfa*. We detected the expression of both *tfec* and *mitfa* in Cluster 13 (**Fig. 4D,E,F**). Additionally, Cluster 13 significantly expressed *tfap2e*, *gpx3*, and *trpm1b* (**Fig. S3**) whose expression patterns have been previously reported in pigment progenitors (Saunders et al., 2019). Finally, a population of pigmented muscle (Cluster 9) was also found with a weak melanophore signature, coupled with expression of muscle markers like *ckmb*, *tpma*, *tnnc2*, and *tnnt3b* (**Fig. S3**; **Fig. S4**).

We next performed wholemount HCR to assess the spatial expression of *mitfa*, *tfec*, and *xdh* during the embryonic to larval transition and to strengthen the validity of our data sets. When examining *mitfa* and *tfec* along the lateral aspects of embryos at 48-50 hpf (**Fig. 4H**), we detected GFP^+ cells that expressed *mitfa*, identifying the melanophores (**Fig. 4H**; white arrowhead), and cells that expressed both *mitfa* and *tfec*, defining the pigment progenitors (**Fig. 4H**; red arrowhead). At 68-70 hpf, we confirmed the four distinct pigment populations we identified through Seurat (**Fig. 4B-G**): GFP^+ melanophores expressing *mitfa* only (**Fig. 4I**; white arrowhead), iridophores only expressing *tfec* (**Fig. 4I**; blue arrowhead), and pigment progenitors expressing both *mitfa* and *tfec* (**Fig. 4I**; red arrowhead) were detected in the larval flank. When examining *xdh* and *mitfa* expression patterns, GFP^+ xanthophores were found to be expressing both markers

(**Fig. 4J**; orange arrowhead), as previously described (Minchin and Hughes, 2008; Saunders et al., 2019).

Taken together, these results show that with our scRNA-seq pipeline we can effectively identify discrete populations based on previously reported cell markers, and coupled with our HCR analysis, effectively show we are able to validate these cell populations.

Mesenchyme in the posterior embryo and larvae exists in various subpopulations

Heatmap analysis of gene expression groups depicted that mesenchyme cells clustered together globally within the data sets (**Fig. 2C,D; Fig. 3C,D; Fig. 5A,B**), with *twist1a* expression broadly labeling all mesenchyme cells (**Fig. 2E,F; Fig. 3E,F**). In addition to *twist1a*, mesenchyme cells also expressed *prrx1a/b, twist1b, foxc1a/b*, *snai1a/b*, *cdh11*, *sparc*, *colec12*, *meox1*, *pdgfra* (**Fig. S3; Fig. 5A,B**), and other known mesenchymal markers such as *mmp2* (**Fig. S3**) (Janssens et al., 2013; Theodore et al., 2017). In whole mount embryos at 48 hpf, we observed broad expression of *foxc1a* and *mmp2* along the posterior pharyngeal arches and ventral regions of the embryo via *in situ* hybridization (**Fig. S7C,D**; arrowheads), confirming their expression territories within posterior-ventral mesenchymal tissues.

Analysis of the Mesenchyme clusters revealed various subtypes were present in the scRNA-seq data sets. Among these, we starkly detected 9 Chondrogenic cell subtypes—Clusters 2, 3, 4, 9, and 12 at 48-50 hpf time point and Clusters 0, 6, 8, and 20 at 68-70 hpf—identified by expression of mesenchymal signature genes, as well as the chondrogenic markers *barx1* and/or *dlx2a* (Sperber et al., 2008) (**Fig. S3; Fig. 5D**). All Chondrogenic clusters expressed *barx1*, regardless of the time point, which is expressed in developing mesenchymal tissues and required for development of osteochondral progenitor cells and their tissue condensation therein (Sperber et al., 2008; Sperber and Dawid, 2008; Ding et al., 2013; Barske et al., 2016). Within the 9 Chondrogenic subtypes, we discovered genes indicative of heterogeneous cell states, ranging from proliferative (Clusters 2, 3, and 12 at 48-50 hpf and Cluster 8 at 68-70 hpf; *cdk1, mcm5,*

mcm6, ccna2, ccnb2, *and/or pcna*), progenitor/stem-like (Cluster 4 at 48-50 hpf; *fen1, uhrf1, id3, chaf1a*), migratory (Cluster 9 at 48-50 hpf and Cluster 20 at 68-70 hpf; *id2a, snai1a, snai2, mmp2*, *and/or twist3*) to differentiating signatures (Clusters 0 and 6 at 68-70 hpf; *col1a2, col5a1, col6a1*, *and/or sparc*) (**Fig. S3**).

All other Mesenchyme subtypes were classified into various progenitor and differentiation categories. Among these categories, 7 clusters expressed either proliferative progenitor makers (Cluster 1 at 48-50 hpf; *pcna, rpa1, mcm5, mcm7*), differentiation signatures (Cluster 6 at 48-50 hpf; *tagln2*, *myl9b*, *aldh1a2*, *actb1*; Cluster 10 at 48-50 hpf and Clusters 17 and 22 at 68-70 hpf; *col2a1a/b, col9a1a, col9a2, col1a2*, and/or *col5a1*), or general migratory mesenchymal markers (Cluster 11 at 48-50 hpf and Cluster 2 at 68-70 hpf; *cxcl12a, cxcl12b, rac1, twist2, snai2 or snai1a*) (**Fig. S3**). Additionally, Cluster 14 at 48 hpf and Clusters 1 and 7 at 68-70 hpf exhibited a general mesenchymal signature, but also expressed Fin Bud marker genes (*hand2, tbx5a, hoxa13a, hoxa13b, hoxd13a, prrx1a/b*, *pcna*) (**Fig. S5**) (Yelon et al., 2000; Lu et al., 2019, Nakamura et al., 2016; Feregrino et al., 2019). The Fin Bud cells formed groupings, as depicted in tSNE analysis (**Fig. S5**), highlighting their distinct transcriptional states from the other mesenchyme populations.

Hierarchical clustering of cells with General Mesenchyme and Chondrogenic identities using a cluster tree further highlighted potential similar subtypes between the time points (**Fig. 5C**). For example, the cluster tree showed proximal location of Cluster 8 at 68-70 hpf and Cluster 2 at 48-50 hpf, which we noted contained clear proliferative chondrogenic gene signatures (**Fig. S3**). Additionally, the tree depicted the closeness of Cluster 1 and 6 at 48-50 hpf with Cluster 2 at 68-70 hpf. These clusters present with varying proliferative/migratory/differentiation states, suggesting that transcriptionally-related mesenchymal cells captured in our data sets were in various stages of dynamic differentiation, proliferation, and migration.

Feature plot exports revealed a sub-distribution of chondrogenic cells (*barx1*$^{+}$) cells in relation to all mesenchyme (*prrx1b*$^{+}$, *twist1a*$^{+}$) cells (**Fig. 5E,L**). To confirm the spatial expression of *prrx1b*, *twist1a*, and *barx1* at 48-50 hpf and 68-70 hpf, we utilized HCR analysis (**Fig. 5F-K,M-**

R). HCR analysis confirmed the expression of *prrx1b*, *twist1a*, and *barx1* within *sox10*:GFP^{+} cells along the posterior pharyngeal arches (white arrowheads) and fin bud mesenchyme (yellow arrowheads) at both time points (**Fig. 5F-K,M-R**). While *prrx1b* and *twist1a* labeled the arches and fin buds (**Fig. 5F,G,M,N**), *barx1* was observed in the arches, but not the fin buds (**Fig. 5I,J,P,Q**), confirming that *barx1* labels a subset of the mesenchyme populations.

Overall, our combined curation, clustering, and HCR analysis has revealed an incredible diversity among the mesenchyme and suggests that mesenchymal cells in the posterior zebrafish exist in various subpopulations and exhibit dynamic transcriptional states during their development. Furthermore, these results show that our analysis pipeline can pinpoint previously unknown discrete subpopulations in complex developing tissues.

Sox10-derived cells during the embryonic to early larval transition reveal enteric progenitor to enteric neuron progression

At 48-50 hpf, cells with neural crest cell identity gene signatures were notably detected in Cluster 5, defined by expression of the markers *sox10, foxd3, crestin*, and *tfap2a* (**Fig. 2C-F; Fig. 6A, Fig. S3**) (Dutton et al., 2001; Luo et al., 2001; Knight et al., 2003; Stewart et. al., 2006). In addition to the core genes, Cluster 5 cells also contained genes previously shown to be expressed in zebrafish neural crest cells; including *vim, snai1b, sox9b*, *zeb2a, mych*, *and mmp17b* (**Fig. 6D**) (Cerdà et al., 1998; Heffer et al., 2017; Hong et al., 2008; Leigh et al., 2013; van Otterloo et al., 2012; Wang et al., 2011; Rocha et al., 2020). We reasoned that many of the neural crest cells had started their respective differentiation programs and were beginning to assume specified genetic profiles. Therefore, we sought to determine if the Neural Crest cell cluster also contained gene expression profiles of known differentiating neural crest cell types along the posterior body, such as enteric neural crest cells (ENCCs).

During neural crest cell diversification, ENCCs fated to give rise to the enteric nervous system (ENS) express a combination of neural crest and enteric progenitor marker genes over developmental time (reviewed in Nagy and Goldstein, 2017; Rao and Gershon, 2018), which occurs between 32 to 72 hpf in zebrafish (reviewed in Ganz, 2018). Enteric markers in zebrafish include *sox10*, *phox2bb*, *ret*, *gfra1a*, *meis3*, and *zeb2a* (Dutton et al., 2001; Shepherd et al., 2004; Elworthy et al., 2005; Delalande et al., 2008; Heanue and Pachnis, 2008; Uribe and Bronner, 2015). Given the developmental timing of early ENS formation in zebrafish as occurring between 32 to 72 hpf, we expected to capture a population of ENCCs within our 48-50 hpf data set. Indeed, within Cluster 5 we observed expression of the enteric markers *phox2bb, ret, gfra1a, meis3, sox10*, and *zeb2a* (**Fig. 6B-D**). Using wholemount *in situ* hybridization, we confirmed the expression of *sox10* and *phox2bb* within ENCCs along the foregut via at 48 hpf (**Fig. S7**; arrowheads). Furthermore, gene orthologs known to be expressed in ENCC in amniotes were detected within this cluster, such as *ngfrb* (orthologue to p75) (Anderson et al., 2006; Wilson et al., 2004) and *hoxb5b* (orthologous to *Hoxb5*) (Kam and Lui, 2015; Kam et al., 2014; Jarinova et al. 2008) (**Fig. 6B-D; Fig. S3**).

HCR analysis of 48 hpf embryos validated the co-expression profiles of several ENCC markers along the foregut (**Fig. 6E-F**; foregut in grey box). Co-expression analysis demonstrated that a chain of *crestin*$^{+}$ cells localized in the foregut contained a subpopulation of cells expressing *ngfrb*, *phox2bb*, and *gfra1a* (**Fig. 6E**; white arrowheads), or expressing *foxd3*, *ngfrb*, and *gfra1a* (**Fig. 6F**; white arrowheads). Together, these HCR data reveal for the first time a quadruple positive population of ENCCs within the zebrafish gut, confirming ENCC markers are co-expressed.

We next asked if we could resolve discrete differentiating enteric neurons over time (**Fig. 7**). In zebrafish, by 72 hpf ENCCs have migrated throughout the length of the gut and begun early neuron differentiation and neural patterning (Elworthy et al., 2005; Olden et al., 2008; Harrison et

al., 2014; Uribe and Bronner, 2015; Taylor et al., 2016). During early neuronal differentiation, ENCCs display differential enteric progenitor gene expression patterns (Taylor et al., 2016) and neurochemical signatures representative of varying stages of neuronal differentiation and subtype diversification (Poon et al., 2003; Holmqvist et al., 2004; Uyttebroek et al., 2010). Zebrafish early differentiating enteric neurons have been characterized by the RNA expression of *sox10*, *phox2bb*, *gfra1a*, *fgf13b*, and *ret,* as well as the immunoreactivity of Elavl3/4 (Shepherd et al., 2004; Heanue and Pachnis, 2008; Uyttebroek et al., 2010; Taylor et al., 2016). In addition, at this time, enteric neurons express multiple neurochemical markers, with Nos1 being most prominent (Olden et al., 2008; Uyttebroek et al., 2010), a finding consistent with studies performed within the amniote ENS (Hao and Young, 2009; Matini et al., 1995; Qu et al., 2008; Heanue et al., 2016). In light of these previous observations, our 68-70 hpf data set was expected to contain the transcriptomes of ENCCs captured at various stages of their progressive differentiation into the diverse subtypes of the ENS.

tSNE analyses identified differentiating enteric neurons within the 68-70 hpf data set based off of the combinatorial expression of *elavl3, phox2bb, ret,* and *gfra1a* (**Fig. 7A**), which mapped to the Neural/Neuronal Major Cell Type regions of the data set (**Fig. 3D**), comprising Clusters 5 and 12 (**Fig. 3B**). Transcripts that encode for the neurochemical marker *nos1,* and the neuropeptides *vip* and *vipb,* a paralogue to *vip* (Gaudet et al., 2011), were found in a subpopulation of enteric neurons localized to a distal group of the Neuronal cluster, likely indicative of a differentiating enteric neuron subtype (**Fig. 7A**; red arrows; **Fig S6**). We then queried for the presence of a combination of pan-neuronal and enteric neuron markers (**Fig. 7B**). Notably, the pan-neuronal markers *tuba2, elavl3, stx1b,* and *gng2/3,* as well as the autonomic neuron markers, *phox2a* and *phox2bb* (Gou et al., 2018; Hans et al., 2013), were present in both Clusters 5 and 12 (**Fig. 7B**). However, the enteric neuron markers, *gfra1a, ret, hoxb5b, ngfrb, fgf13b, nos1, vipb,* and *vip* were mostly confined to Cluster 12, suggesting that this cluster

contained differentiating enteric neurons (**Fig. 7B**). Indeed, HCR analysis validated the spatiotemporal expression of *phox2bb, nos1, vipb,* and *elavl3* transcripts in ENCCs throughout the foregut of the zebrafish embryo by 69 hpf (**Fig. 7C**; yellow arrowheads). These results suggest that *elavl3*$^{+}$/*phox2bb*$^{+}$ early differentiating enteric neurons in the foregut display an inhibitory neurochemical signature, consistent with prior observations in zebrafish and mammalian ENS (Olden et al., 2008; Hao and Young, 2009).

In an effort to examine the enteric neuron populations with finer resolution, Clusters 5 and 12 were subset from the main data set in Seurat, re-clustered and visualized using a tSNE plot, producing 5 new clusters (**Fig. 7D**). The top significantly expressed markers from each new Sub-Cluster are provided in **Table S2**. Following this, the previously mentioned enteric neuron markers, with the addition of *etv1,* a recently identified marker of enteric intrinsic primary afferent neurons (IPANs) in mouse (Morarach et al., 2020), were queried and visualized using dot and feature plots allowing the identification of Sub-Cluster 4 as a differentiated enteric neuron cluster (**Fig. 7E-F**). Both *nos1* and *vipb* were enriched in Sub-Cluster 4 (**Fig. 7G**). Interestingly, while expressed at lower average levels than in Sub-Cluster 4, the enteric combination markers were also present in Sub-Cluster 1 (**Fig. 7E,G**). Sub-Cluster 1 formed a central point from which Sub-Cluster 4 could be seen emanating as a distal population (**Fig. 7D**). Given the developmental timing, this is likely depicting enteric neurons captured at different stages along their progressive differentiation, which would suggest that the distal most population represents the more mature enteric neurons (**Fig. 7D-E**).

Given our hypothesis that the enteric neurons further along a differentiation program were localized to the distal tip of Sub-Cluster 4, we asked whether this population of cells contained additional neurochemical or neuron subtype specific differentiation genes. As expected, a small pocket of these cells was found to contain the two acetylcholine associated genes, acetylcholine esterase (*ache)* (Bertrand et al., 2001; Huang et al., 2019) and vesicular acetylcholine transferase

(*slc18a3a*) (Hong et al., 2013; Zoli, 2000) (**Fig. 7G**; red arrowheads). Within Sub-Cluster 4, we detected the expression of *calb2a* and *pbx3b* (**Fig. 7G**), two genes that have previously been shown to specify myenteric IPANs in mammals (Furness et al., 2004; Memic et al., 2018). Corroborating our single-cell findings, HCR analysis revealed the co-expression of *pbx3b, calb2a, vipb, nos1,* and *slc18a3a* in discrete enteric neurons within the foregut region of the zebrafish gut at 68 hpf (**Fig. 7H**). In particular, *calb2a, vipb, nos1,* and *slc18a3a* were all found to be co-expressed (**Fig. 7H**; yellow arrowheads). While *pbx3* expression was found in combination with *calb2a, vipb, and nos1* (**Fig. 7H**; white arrowheads), in agreement with our transcriptome data (**Fig. 7G**), we were unable to observe detectable levels of *slc18a3a* within the *pbx3b* expressing cells.

Taken together, these data regarding enteric neuron subpopulations suggest a model (**Fig. 7I**), whereby *nos1, vipb, calb2a,* and *pbx3b* are co-expressed within early enteric neurons, and that through lineage-restricted gene expression, *pbx3b* expression may promote the assumption of an IPAN signature characterized by the presence of *calb2a, ache,* and *slc18a3a* and the loss of inhibitor markers *nos1* and *vipb*. Therefore, our single-cell analysis in zebrafish suggests that the transcriptional emergence of specific enteric neuron subtypes may be conserved between vertebrate species.

Atlas of sox10:GFP^{+} cell types encompassing the embryonic-to-larval transition

To describe the dynamic relationship between the *sox10*:GFP^{+} cells across both time points, we merged the 48-50 hpf and 68-70 hpf data sets using Seurat's data set and Integration and Label Transfer utility (Stuart et al., 2019). The merged data sets were visualized via UMAP (Becht et al., 2019; Mcinnes et al., 2018), which allowed us to describe the transition between cell types by making both inter- and intra-cluster comparisons. After integrating the two data sets, we observed that every cluster identified in the 48-50 hpf data set mapped proximally to clusters at 68-70 hpf (**Fig. S8A**).

We next labeled each cell using the Major Cell Type categories: Neural, Neuronal, Glial, Neural Crest, Pigment, Mesenchyme, Otic, and Muscle, as in Fig. 2 and 3, forming a major cell type Atlas across both time points (**Fig. S8B**). Further refinement of these cell identities based on our previous curation (**Fig. S3**) allowed us to form a higher resolution Atlas for each cell type (**Fig.8A**). The top significantly enriched markers for each major cell type category in the Atlas is provided in **Table S3**. The overall architecture of the UMAP revealed that the cells of each major cell type congregated together, which strongly supports that our formerly described characterizations of each time point are accurate and predictive. For example, cells with Mesenchyme identity constellated together, forming three large Mesenchyme regions in the Atlas: General, Chondrogenic, and Fin bud (**Fig. 8A,B**). Neural crest cells mapped precisely to the top end of a Neural/Neuronal region of the Atlas, which then transitioned into Schwann cells laterally and differentiating neurons at the base (**Fig. 8A,D**). Additionally, Pigment cell types aligned adjacent to one another in the Atlas (**Fig. 8A,C**). Validation of cellular subtypes within the Atlas can be found in the supplement **Fig. S8D**. Overall, these concurrent cluster regions not only support our previous characterizations of each cell type, but also function as an informative resource data set for the scientific community (**Fig. S8C**).

Comparison of individual subsets of clusters may provide deeper analysis of each cell type, with respect to changing cell states across time. To explore this, we examined three of the largest regions of the Atlas in detail: Mesenchyme, Pigment, and Neural/Neuronal cell types.

We observed a remarkable consistency across the larger Mesenchyme population, which excluded the Fin bud mesenchyme, in both the cluster identity shown in the UMAP and gene expression profiles. First, we examined cells in the main Mesenchyme clusters (**Fig. 8B**); 9 clusters (Clusters 1-4, 6, 9-12) originated from the 48-50 hpf data set and 5 clusters (Clusters 0,2,6,8, and 20) derived from 68-70 hpf. For example, 48h-Cluster 2 and 68h-Cluster 8 both showed a very high degree of similarity, as well as consistent *barx1, dlx2a*, and *twist1a* expression, consistent with our prior analysis (**Fig. 5**). Further, 48h-Clusters 11 and 12 shared a

common identity with 68h-Cluster 0, as noted by the strong expression of both *foxc1a*, and *prrx1b*. Lastly, 48h-Clusters 1, 6, 9, and 10 overlapped with 68h-Clusters 2, 6, and 20, marked by their common expression of *snai1a* (**Fig. 8B**).

The central node of the Pigment region within the Atlas was marked by the 48h-Cluster 8, which resolved into respective pigment chromatophore clusters at 68-70 hpf (**Fig. 8C**). We were able to globally discern that pigment cell types displayed expression of *sox10*, regardless of time point. In particular, as expected from our previous analysis, we observed the early specified melanophore population at 48h-Cluster 8 branched into later stage melanophore populations (69h-Clusters 4 and 18), both of which expressed *mitfa* and *dct*. Further, we observed that the common bi-potent pigment progenitor population (68h-Cluster 13) bridged both melanophore clusters and the iridophore 68h-Cluster 16; we observed that the iridophores, marked by *tfec* and *gpnmb*, segregated distinctly away from the melanophores. This nested positioning of 68h-Cluster 13 supports its dual progenitor identity. Lastly, Xanthophores, marked by *xdh*, segregated tightly away from the remaining pigment populations, reflective of their earlier and distinct lineage (**Fig. 4A**).

Cells within the Neural/Neuronal clusters of the Atlas self-organized such that progenitor cells bridged into differentiating neurons spatially from the top to the bottom of the Neural/Neuronal region of the Atlas (**Fig. 8D**). Within this region, 6 clusters (Clusters 0, 5, 7, 13, 15, 17) were represented from 48-50 hpf, and 5 clusters (Clusters 3, 5, 10, 12, 14) from 68-70 hpf. The 68-70 hpf Neural progenitor populations (Clusters 3 and 10) shared common gene expression with the 48-50 hpf Neural Crest population (48h-Cluster 5), reflected largely by their co-expression of *sox10*, *notch1a*, *dla*, and *foxd3* (**Fig. 8D; Fig. S8D**). We confirmed the spatiotemporal expression domains of *notch1a* and *dla* along the hindbrain, spinal cord, and in NCC populations along the post-otic vagal domain at 48 hpf (**Fig. S7E,F**; arrowheads), in particular with *dla* in the ENCCs along the foregut (**Fig. S7F**; arrow), a pattern similar to the ENCC

makers *sox10* and *phox2bb* (**Fig. S7A,B**). Delineated from the Neural progenitor cells, we observed a bifurcation in the cell states; with one moving towards a Schwann/Glial cell fate, while the other branched towards Neuronal. The Glial arm followed a natural progression of earlier cell fates at 48-50 hpf (48h-Cluster 15) toward the more mature fates at 68-70 hpf (68h-Cluster 14). Together, these Glial fates were denoted by the expression of *olig2* and *pou3f1*, respectively. Beginning with 48h-Cluster 13, we observed the beginning of the neuronal populations, namely 48h-Clusters 0, 7, 13, and 17 and 68h-Clusters 5 and 12. Cells in these clusters patterned in the Atlas UMAP such that the progenitor clusters (48h-Clusters 0, 13, and 17; 69h-Cluster 5) form a spectrum of cell states leading toward the neuronal populations (48h-Cluster 7; 69h-Cluster 12). Among the Neuronal populations, we observed a clear autonomic signature, indicated by *phox2a* and *phox2bb* (**Fig. 8D; Fig. S8D**). More strikingly, we also detected a large fraction of enteric progenitors, indicated by *ret, ngfrb,* and *hoxb5b* expression, (**Fig. 8D; Fig. S8D**) supporting our previous observations (**Fig. 6-7**). The enteric progenitors culminated into a pool of enteric neurons, with the specific neural signature: *vipb, nos1, gfra1a, fgf13b,* and *etv1* (**Fig. 8D; Fig. S8D**). Together, these data corroborate our previous findings (**Fig. 7**) through a secondary reassessment of our data sets and they generate a catalogued Atlas resource for the community to use for their own research questions regarding *sox10*-expressing and *sox10*-derived cells.

A hox gene signature within sox10-derived cells in the posterior fish

A common theme examined by many recent and insightful single cell profile studies of the neural crest (Dash and Trainor, 2020; Soldatov et al., 2019) is that *hox* genes display marking expression patterns. *Hox* genes are uniquely suited to help provide spatial information about the cells within our data sets as the expression of *hox* genes strongly correlates with discrete rostral-to-caudal positions (Dash and Trainor, 2020). To analyze if we could detect *hox* gene patterns within our own data set, we queried all the known canonical *hox* genes within zebrafish as listed on zfin.org (Ruzicka et al., 2019). We detected broad expression of 45 *hox* genes across the Atlas

(**Fig. 9A,B**), which identified all but four genes (*hoxc1a*, *hoxc12b*, *hoxa11a*, and *hoxa3a*), which were not examined further.

Several trends quickly emerged within the Atlas between discrete *hox* expression signatures and select cell types. A core *hox* profile demarcated the general Neural/Neuronal identities, which included; *hoxa4a*, *hoxb1b*, *hoxb2a*, *hoxb3a, hoxb5a, hoxb5b, hoxc1a*, *hoxc3a, hoxd3a*, and *hoxd4a* (**Fig. 9A,C**). This core *hox* signature applied generally to the Neural Crest, Neural Progenitors, Enteric Progenitors, Enteric Neurons, Glial progenitors, Autonomic neuronal progenitors, and CNS neurons within the Atlas. Generally, these *hox* genes are expressed strongest in the pre- and post-otic regions, with particular enrichment in the hindbrain/vagal axial domains, though expression can be detected posteriorly (Veraksa et al., 2000; Barsh et al., 2017). While Glial fates, encompassed by the Glial progenitors and Schwann cells, retained the *hox* pattern, they exhibited overall decreased *hox* expression, when compared with Neuronal populations (**Fig. 9A**). The *hox* gene Neural/Neuronal signature likely correlates with the discrete spatial vagal-level and anterior spinal cord-level domains within which the populations originate and also provides a ground work for further experimental validation of the combinatorial role the *hox* genes may play in differentiation of NCC-derived neural cell fates in the posterior embryo.

While a common Neuronal/Neural *hox* signature was evident among *sox10*:GFP^{+} cells, further inspection of the Atlas revealed several subtle, yet distinct signatures which distinguish several cell types. First, when considered with the general neural *hox* signature, it was possible to distinguish the enteric fated cells purely by their *hox* code. The enteric progenitors and enteric neurons were segregated from the other neural groups based on their uniquely strong expression of *hoxa5a* (**Fig. 9D**). Moreover, both enteric groups lacked strong expression for *hox* genes that marked other neurons, such as *hoxa9a, hoxb7a, hoxb10a*, *hoxc1a,* and *hoxc5a* (**Fig. 9A,F,G**). Secondly, while Autonomic neuronal progenitors did not deviate largely from the general neural *hox* signature, they also displayed prominent enrichment of *hoxa4a*, *hoxc5a*, and *hoxc6a*. A CNS

signature was broadly evident within the general neural signature, with representation of most *hox* genes, including the genes *hoxa9a*, *hoxd10a*, and *hoxd10a*, factors which are expressed posterior to the vagal axial region. Overall, the *hox* gene signatures highlight the axial specificity of both the general autonomic and enteric *hox* signatures within the *sox10* Atlas.

With respect to the remaining cluster identities (**Fig. 9A**), many of the populations showed varied *hox* expression profiles. Both the Chondrogenic and General Mesenchyme clusters demonstrated *hoxa2b* expression, as well as weak expression for *hoxb2a, hoxb3a*, and *hoxd4a*. Our detection of these *hox* expression profiles was consistent with prior reports that they are expressed within NCC targets toward the posterior pharyngeal arches, as well as migrating NCC (Minoux and Rijli, 2010; Parker et al., 2018, 2019). We detected the distinct identity of the Fin Bud mesenchyme (Ahn and Ho, 2008; Nakamura et al., 2016) through the expression of *hoxa9b, hoxa10b, hoxa11b, hoxa11b, hoxa13b*, *hoxd9a,* and *hoxd12a* (**Fig. 9A,E**). The pigment populations, including the Pigment progenitors, Melanophores, Iridophores, and Xanthophores, contained generally low levels of *hox* gene expression. Despite this, we still observed a slight variation of *hox* expression among the pigment populations. For example, low levels of *hoxa4a*, *hoxb7a*, *hoxb8a*, *hoxc3a*, and *hoxd4a* were detected among the Iridophore population, while only *hoxb7a* was detected within a high fraction of Xanthophores (**Fig. 9A,G**). Interestingly, these expression profiles are not shared by the Melanophore population, which displayed uniformly very low levels of detectable *hox* expression. Lastly, the Muscle, Otic Epithelium, and Unidentified cells showed almost no *hox* expression profile, which serves a foil for the specificity of the signatures outlined. We noted that the “Pigmented Muscle” cluster weakly mirrored the general neural *hox* signature, likely a shared signature more reflective of the axial position of the muscle cells rather than a shared genetic profile, as corroborated by their distinct separation of the clusters on the UMAP.

Overall, these above described *hox* signatures detected within our scRNA-seq Atlas suggests that distinct cell types may utilize unique *hox* combinations during their delineation. Furthermore, these data highlight the specificity and integrity of our cell identity curation, without which we would not be able to identify these remarkably distinct *hox* signatures. Description of the *hox* signatures within this Atlas provides further tools to identify these discrete cell populations, as well as exciting new avenues for further mechanistic investigation.

DISCUSSION

We present a single cell transcriptomic Atlas resource capturing the diversity of posterior-residing *sox10*-derived cells during the embryonic (48-50 hpf) to early larval transition (68-70 hpf) in zebrafish. From our analysis, we identified a large number of neural crest-derived cell types; including pigment progenitor cells delineating into distinct chromatophores, as well as neural crest, glial, neural, neuronal, and mesenchymal cells at high resolution, extending prior whole embryo-based zebrafish single cell studies (Farnsworth et al., 2020) and expanding the resolution at which these cells have been described to date. We discovered that distinct *hox* transcriptional codes demarcate differentiating neural and neuronal populations, highlighting their potential roles during cell subtype specification. We also uncovered evolutionarily-conserved transcriptional signatures of differentiating enteric neuron cell types, thereby expanding our knowledge of enteric nervous system development. Corroborating our transcriptomic characterizations, we validated the spatiotemporal expression of several key cell type markers using HCR. Furthermore, our data sets captured otic vesicle and muscle cells, populations which the *sox10:*GFP line has been characterized as marking, and may be useful for investigating these cell types in the future.

Collectively, this comprehensive cell type Atlas can be used by the wider scientific community as a valuable resource for further mechanistic and evolutionary investigation of *sox10*-expressing and neural crest-derived cells during development and the ontogenesis of neurocristopathies.

Analysis of pigment populations demonstrated the accuracy and specificity of our transcriptome data sets and identified distinct neural crest-derived differentiating chromatophore lineages during the embryonic to larval transition, extending on previous descriptions of pigment cell lineage development performed in older larval and juvenile zebrafish at single cell resolution (Saunders et al., 2019). Specific markers for each chromatophore population have been documented at different time points during zebrafish development (Higdon et al., 2013; Petratou et al., 2018, 2019; Saunders et al., 2019), including *mitfa*, *tfec*, *atic*, and *xdh*, thus serving as a touchstone to validate both the precision and consistency of our analysis pipeline (**Fig. 4**). Specifically, melanophores (Cluster 8) were identified in the 48-50 hpf data set (**Fig. 4B,C**), while at 68-70 hpf we identified iridophore, xanthophore, pigment progenitor, and two distinct melanophore populations (**Fig. 4D-G**). We employed the robust characterization of these pigment populations to validate technical aspects of integrating both time points into a single, cohesive Atlas (**Fig. 8A**). The Atlas UMAP shows a common progenitor population branching into both the iridophores and the melanophores, which are composed of the melanophore progenitor cluster from 48-50 hpf and the two melanophore clusters at 68-70 hpf (**Fig. 8C**). We validated the results regarding pigment population gene signatures using wholemount HCR on 48-50 hpf and 68-70 hpf embryos (**Fig. 4 H-J**). Thus, our validation of pigment populations highlights that the *sox10* Atlas can be used to identify cell lineages and discover new information regarding their development in zebrafish.

Our data sets captured the transition from enteric neural progenitor to differentiating enteric neuron subtype (**Fig. 6,7,8**). We found that in both 48-50 and 68-70 hpf data sets, the expression of *elavl3*, *phox2bb*, *ret*, and *gfra1a* transcripts were present (**Fig. 6,7**); however,

enteric progenitor populations at 48-50 hpf still retained a neural crest signature, marked by *crestin* and *foxd3*, among others (**Fig. 6**). The combined Atlas revealed broad transcriptional states captured within enteric neural progenitors and enteric neurons (**Fig. 8D**), whereby *elavl3*, *phox2bb*, *ret*, *ngfrb*, and *gfra1a* could be seen extending throughout the Neural/Neuronal regions of the Atlas. A similar enteric progenitor population consisting of *Sox10*, *Ret*, *Phox2b*, and *Elavl4* was identified by scRNA-seq in the mouse (Lasrado et al., 2017), indicating zebrafish express conserved enteric programs. Notably, genes that encode for neurochemicals within enteric neurons were detected in the enteric clusters, with *nos1* and *vipb* being most prominent (**Fig. 8D**) and co-expressed in a subset of cells among the enteric neuron population along the foregut (**Fig 7A-C**). Collectively, these results regarding enteric populations suggest that the Atlas likely reflects cells captured across a spectrum of differentiation states, with immature neurons reflecting the onset of *elavl3* expression, while others, such as the *nos1*$^{+}$/*vipb*$^{+}$ subpopulation, representing cells further along a differentiation trajectory.

A recent scRNA-seq study performed using E15.5 mice, a time point further along in ENS development when compared to our zebrafish study described here, suggests that *Nos1*$^{+}$/*Vip*$^{+}$ cells represent a post-mitotic immature neuron population capable of branching into excitatory and inhibitory neurons via subsequent differentiation mediated by lineage-restricted gene expression (Morarach et al., 2020). Their model posits that *Nos1*$^{+}$/*Vip*$^{+}$/*Gal*$^{+}$ enteric neurons are capable of assuming an intrinsic primary afferents neuron (IPAN) signature, characterized by the loss of *Vip* and *Nos1*, and the gain of *Calb*, *Slc18a2*/*3*, and *Ntng1*; a process regulated by transcription factors, *Pbx3* and *Etv1*. This model of IPAN formation appears congruent with a previous birth dating study performed in mice, where researchers demonstrated the transient expression of *Nos1* in enteric neurons (Bergner et al., 2014). We wondered if the IPAN gene expression signature was evolutionarily conserved in zebrafish. Testing this spatiotemporal gene signature model in our own data sets, we asked if the *nos1*$^{+}$/*vipb*$^{+}$ population represented a

snapshot of immature enteric neurons. We found that *pbx3b*, *etv1*, *calb2a*, *slc18a3a*, *ache*, *vipb*, and *nos1* were all expressed in differentiating enteric neuron clusters (**Fig. 7F-G; Fig. S6A**), likely reflecting their transition to an IPAN fate in our 68-70 hpf data set. Intriguingly, we discovered that the markers tightly mapped to a subpopulation of cells in an enteric neuron sub-cluster (**Fig. 7G**, red arrows) and that *nos1* was either absent or expressed at lower levels than other enteric subpopulations (**Fig. 7F; S6A**), a finding that corroborates the proposed mammalian model. Our observations in zebrafish suggest that we captured a transitional time point where subsequent differentiation is just being initiated and suggests an evolutionarily-conserved mechanism of ENS formation across vertebrate species.

The study of neural crest-derived posterior cell types has recently gained increased attention due to their complex and essential roles in vertebrate development (Gandhi et al., 2020; Hutchins et al., 2018; Soldatov et al., 2019; Ling and Sauka-Spengler, 2019). Characterizing the differentiation of neural crest-derived cells is important to understand as it will enhance our concept of human health, especially to fields such as stem cell therapeutics and regenerative medicine. While prior studies provide incredible insight into their own respective research systems, our paper is the first single-cell transcriptomic analysis covering detailed description of the early development of enteric nervous system in fish, in addition to a high resolution analysis of the *sox10*$^{+}$ mesenchyme and pigment cells present during the late embryonic to larval phase. The developmental window we examined, the embryonic to larval transition, is regarded as an ephemeral phase (Singleman and Holtzman, 2014) and as such is expected to contain the dynamic cell differentiation states that we observed within our Atlas. Indeed, our identification of diverse cell states among the neural crest-derived cells mirrors cell types and transcriptional signatures detected in amniote embryos across comparable time points (Soldatov et al., 2019; Ling and Sauka-Spengler, 2019), extending the same powerful insight to the zebrafish model and

suggesting the regulatory mechanisms that dictate cell fate specification are conserved between anamniotes and amniotes.

In summary, our study greatly increases our foundational understanding of neural crest-derived cell fates, as well as other *sox10*$^{+}$ posterior cell types in zebrafish, thereby complementing ongoing studies in mammalian models and expanding fundamental knowledge of how cells diversify in developing organisms. The spatiotemporal information contained within our zebrafish Atlas will serve as a resource for the developmental biology, stem cell, evolutionary biology and organogenesis communities.

METHODS & MATERIALS

Animal Husbandry, Care, & Synchronous Embryo Collection

Adult *Tg(-4.9sox10:GFP; ba2Tg)* (Carney et al., 2006) zebrafish (*Danio rerio*) were bred to generate synchronously staged embryos across several clutches. All embryos were cultured in standard E3 media until 24 hours post fertilization (hpf), then transferred to a 1X 1-phenyl 2-thiourea (PTU)/E3 solution (Karlsson et al., 2001), to arrest melanin formation. Embryos were manually sorted for GFP expression and synchronously staged at 24 hpf. Embryos which exhibited developmental delay or other defects were removed. All work was performed under protocols approved by, and in accordance with, the Rice University Institutional Animal Care and Use Committee (IACUC).

Isolation of Tissue & Preparation of Single Cell Suspension

Embryos between 48-50 hpf and/or larvae between 68-70 hpf were dechorionated manually and then transferred to 1X sterile filtered PBS, supplemented with 0.4% Tricane (Sigma, A5040) to anesthetize. Tissue anterior to the otic vesicle and tissue immediately posterior to the anal vent was manually removed using fine forceps in 48-50 hpf embryos, while only tissue anterior to the otic vesicle was removed from 68-70 hpf larvae, as schematized in Fig. 1. Remaining tissue segments were separated into nuclease-free eppendorf tubes and kept on ice immediately following dissection. Dissections proceeded over the course of 1 hour. To serve as control for subsequent steps, similarly staged AB WT embryos were euthanized in tricaine and then transferred to sterile 1X PBS. All following steps were conducted rapidly in parallel to minimize damage to cells: Excess PBS was removed and tissue was digested in 37°C 1X Accumax buffer (Sigma-Aldrich, A7089) for 30-45 minutes to generate a single cell suspension for each sample. Digestion was monitored very closely for total suspension of all tissue. At 10 minute intervals, tissue was gently manually disrupted with a sterile pipette tip. Single cell suspensions were then transferred to a fresh chilled sterile conical tube and diluted 1:5 in ice cold Hank's Buffer (1x

HBSS; 2.5 mg/mL BSA; 10μM pH8 HEPES) to arrest the digestion. Cells were concentrated by centrifugation at 200 rcf for 10 minutes at 4°C. Supernatant was discarded carefully and cell pellets were resuspended in a small volume of Hank's Buffer. Cell solution was passed through a 40 μm sterile cell strainer to remove any remaining undigested tissue and then centrifuged as above. Concentrated cells were resuspended in ice cold sterile 1X PBS and transferred to a tube suitable for FACS kept on ice.

Fluorescent Cell Sorting, & Single Cell Sequencing

Fluorescent Assisted Cell Sorting (FACS) was performed under the guidance of the Cytometry and Cell Sorting Core at Baylor College of Medicine (Houston, TX) using a BD FACSAria II (BD Biosciences). Zebrafish cells sorted via GFP fluorescence excited by a 488 nm laser, relying on an 85 μm nozzle for cell selection. Detection of GFP^+ cells was calibrated against GFP^- cells collected from AB wildtype embryos, as well as GFP^+ cells collected from the anterior portions of the *sox10:*GFP embryos.

Sample preparation for scRNA-seq was performed by Advanced Technology Genomics Core (ATGC) at MD Anderson (Houston, TX). FACS-isolated cells were run on a 10X Genomics Chromium platform using 10X Single Cell 3' V2 chemistry kit for 10,000 cells. Sequencing of libraries was conducted on an Illumina NextSeq500. Sequencing was aligned at MD Anderson ATGC to the DanioGRCz10 version of the zebrafish genome using the 10X Genomics Cell Ranger software (v2.1.0) (Zheng et al., 2017). Mitochondrial genes were regressed out from the data set during the Cell Ranger alignment. Gene reads per cell were stored in a matrix format for further analysis.

Data Processing & Analysis

The 10x genomics sequencing data was then analyzed using Seurat (Satija et al., 2015, Stuart et al. 2019, Butler et al., 2018) v3.1.1 software package for R, v3.6.3 (R Core Team, 2020). The standard workflow was followed for data processing. Briefly, for both the 48-50 hpf and 68-70 hpf

data sets, cells which contained low (<200) or high (>2500) genes were removed from analysis. Gene expression was normalized using the NormilizeData command, opting for the LogNormalize method (Scale factor set at 10,000) and further centered using the ScaleData command. Variable features of the data set were calculated with respect to groups of 2,000 genes at a time. Both data sets were evaluated considering the first 20 principle components (PC) as determined by the RunPCA command with a resolution of 1.2 for PCA, tSNE, and UMAP analyses. The appropriate PCs were selected based on a Jack Straw analysis with a significance of $P < 0.01$. Clustering was performed using FindNeighbors and FindClusters in series. We identified 19 clusters in the 48-50 hpf data set and 23 clusters in the 68-70 hpf data set. All cluster identities were carefully manually curated via combinatorial expression analysis of published marker genes. Generation of the merged Atlas was performed via the FindIntegrationAnchors workflow provided in the Standard Workflow found on the Seurat Integration and Label Transfer vignette. Clustering was performed for the Atlas based on the first 20 PCs, consistent with the original data sets. Subsets of the Atlas in Fig. 8B-D discounted any spuriously sorted cells for clarity. All features plots represent expression values derived from the RNA assay. Subclustering of the enteric neurons was performed by subsetting clusters 5 and 12 from the 68-70 hpf data set and reinitializing the Seurat workflow, as described above. Clusters were identified based on the first 6 PCs. Detection of cell cycle phase was conducted following the Cell cycle and scoring vignette. Genes used for identification of cell cycle phases can be found in the supplementary table (Fig. S2). Dendrograms rely on Seurat's BuildClusterTree function.

Whole mount in situ Hybridization

cDNAs for *foxc1a*, *notch1a*, and *dla* were amplified via high fidelity Phusion-HF PCR (NEB) from 48 hpf AB WT cDNA libraries using primers in Fig. S9A. PCR products were cloned using the Zero Blunt™ TOPO™ PCR Cloning Kit (Invitrogen), as per manufacturer protocols, and sequenced validated. Plasmids encoding *phox2bb*, *sox10*, *mmp2* were generously sourced as

listed (Fig. S9A). Antisense digoxigenin (DIG)-labeled riboprobes were produced from cDNA templates of each gene. AB wild type embryos were treated and stained to visualize expression as previously described in (Jowett and Lettice, 1994). Following *in situ* reactions, embryos were post-fixed in 4% Paraformaldehyde (PFA) and mounted in 75% Glycerol for imaging. A Nikon Ni-Eclipse Motorized Fluorescent upright compound microscope with a 4X objective was used in combination with a DS-Fi3 color camera. Images were exported via Nikon Elements Image Analysis software.

Whole mount Hybridization Chain Reaction

HCR probes were purchased commercially (Molecular Instruments Inc., CA) and were targeted to specific genes based on their Ref Seq ID (Fig. S9B). Wholemount HCR was performed according to the manufacturer's instructions (v3.0, Choi et al., 2018, Choi et al., 2016) on *sox10:*GFP^{+} embryos previously fixed at the appropriate stage in 4% PFA. All embryos were cleared in >70% glycerol prior to imaging.

Confocal Imaging & Image Processing

Prior to imaging, embryos were embedded in 1% Low melt agarose (Sigma) and were then imaged using an Olympus FV3000 Laser Scanning Confocal, with a UCPlanFLN 20×/0.70 objective. Confocal images were acquired using lambda scanning to separate the Alexafluor 488/Alexafluor 514 or the Alexafluor 546/Alexafluor 594 channels. Final images were combined in the FlowView software and exported for analysis in either Fiji (Rueden et al., 2017; Schneider et al., 2012; Schindelin et al., 2012) or IMARIS image analysis software (Bitplane). Figures were prepared in Adobe Photoshop and Illustrator software programs, with cartoons created via BioRender.com.

ACKNOWLEDGEMENTS

Funding for this project was provided by Rice University, Cancer Prevention & Research Institute of Texas (CPRIT) Recruitment of First-Time Tenure Track Faculty Members (CPRIT-RR170062) and the NSF CAREER Award (1942019) awarded to R.A.U., a Houston Livestock Show & Rodeo Research Award to J.A.M. and P.A.B., and a SDB Choose Development! Fellowship award to J.L.W. We acknowledge the Cytometry and Cell Sorting Core at Baylor College of Medicine, which is funded from the CPRIT Core Facility Support Award (CPRIT-RP180672), the NIH (P30 CA125123 and S10 RR024574), and the expert assistance of Joel M. Sederstrom for assistance with flow cytometry. Single cell library preparation, Illumina sequencing, and Cell Ranger alignment was facilitated by Advanced Technology Genomics Core at MD Anderson Cancer Research Center funded by CA016672(ATGC). IMARIS image analysis was performed using Rice University's Shared Equipment Authority (SEA) IMARIS workstation. We thank George Eisenhoffer and Oscar Ruiz (MD Anderson) for advice regarding flow cytometry and single-cell RNA-seq methodology. We thank Sarah Kucenas (University of Virginia) for helpful advice on glial populations. We thank Robert Naja and Robyn Fenty for technical assistance.

Competing Interests: The authors claim no competing interests.

Citations

Ahn, D., and Ho, R.K. (2008). Tri-phasic expression of posterior Hox genes during development of pectoral fins in zebrafish: Implications for the evolution of vertebrate paired appendages. Dev. Biol. *322*, 220–233.

Ahrens, M.B., Orger, M.B., Robson, D.N., Li, J.M., and Keller, P.J. (2013). Whole-brain functional imaging at cellular resolution using light-sheet microscopy. Nat. Methods *10*, 413–420.

Anderson, R.B., Stewart, A.L., and Young, H.M. (2006). Phenotypes of neural-crest-derived cells in vagal and sacral pathways. Cell Tissue Res. *323*, 11–25.

Barlow, A.J. (1984). Neural Crest Cells in Enteric Nervous System Development and Disease. In Neural Crest Cells, (Elsevier Inc.), pp. 101–104.

Barsh, G.R., Isabella, A.J., and Moens, C.B. (2017). Vagus Motor Neuron Topographic Map Determined by Parallel Mechanisms of hox5 Expression and Time of Axon Initiation. Curr. Biol. *27*, 3812–3825.

Barske, L., Askary, A., Zuniga, E., Balczerski, B., Bump, P., Nichols, J.T., and Crump, J.G. (2016). Competition between Jagged-Notch and Endothelin1 Signaling Selectively Restricts Cartilage Formation in the Zebrafish Upper Face. PLoS Genet. *12*, e1005967.

Becht, E., McInnes, L., Healy, J., Dutertre, C.A., Kwok, I.W.H., Ng, L.G., Ginhoux, F., and Newell, E.W. (2019). Dimensionality reduction for visualizing single-cell data using UMAP. Nat. Biotechnol. *37*, 38–47.

Bergner, A.J., Stamp, L.A., Gonsalvez, D.G., Allison, M.B., Olson, D.P., Myers, M.G., Anderson, C.R., and Young, H.M. (2014). Birthdating of myenteric neuron subtypes in the small intestine of the mouse. J. Comp. Neurol. *522*, 514–527.

Bertrand, C., Chatonnet, A., Takke, C., Yan, Y.L., Postlethwait, J., Toutant, J.P., and Cousin, X. (2001). Zebrafish acetylcholinesterase is encoded by a single gene localized on linkage group 7. Gene structure and polymorphism; molecular forms and expression pattern during development. J. Biol. Chem. *276*, 464–474.

Bolande, R.P. (1997). Neurocristopathy: Its Growth and Development in 20 Years. Pediatr. Pathol. Lab. Med. *17*, 1–25.

Bradford, Y.M., Toro, S., Ramachandran, S., Ruzicka, L., Howe, D.G., Eagle, A., Kalita, P., Martin, R., Moxon, S.A.T., Schaper, K., et al. (2017). Zebrafish models of human disease: Gaining insight into human disease at ZFIN. ILAR J. *58*, 4–16.

Brosens, E., Burns, A.J., Brooks, A.S., Matera, I., Borrego, S., Ceccherini, I., Tam, P.K., García-Barceló, M.M., Thapar, N., Benninga, M.A., et al. (2016). Genetics of enteric neuropathies. Dev. Biol. *417*, 198–208.

Butler, A., Hoffman, P., Smibert, P., Papalexi, E., and Satija, R. (2018). Integrating single-cell transcriptomic data across different conditions, technologies, and species. Nat. Biotechnol. *36*, 411–420.

Carney, T.J., Dutton, K.A., Greenhill, E., Delfino-Machin, M., Dufourcq, P., Blader, P., and Kelsh, R.N. (2006). A direct role for Sox10 in specification of neural crest-derived sensory neurons. Development *113*, 4619–4630.

Cerdà, J., Conrad, M., Markl, J., Brand, M., and Herrmann, H. (1998). Zebrafish vimentin: Molecular characterisation, assembly properties and developmental expression. Eur. J. Cell Biol. *77*, 175–187.

Choi, H.M.T., Calvert, C.R., Husain, N., Huss, D., Barsi, J.C., Deverman, B.E., Hunter, R.C., Kato, M., Lee, S.M., Abelin, A.C.T., et al. (2016). Mapping a multiplexed zoo of mRNA expression. Development *143*, 3632–3637.

Choi, H.M.T., Schwarzkopf, M., Fornace, M.E., Acharya, A., Artavanis, G., Stegmaier, J., Cunha, A., and Pierce, N.A. (2018). Third-generation in situ hybridization chain reaction: multiplexed, quantitative, sensitive, versatile, robust. Development *145*, dev165753.

Dash, S., and Trainor, P. (2020). The development, patterning and evolution of neural crest cell differentiation into cartilage and bone. Bone *137*, 115409.

Delalande, J.M., Guyote, M.E., Smith, C.M., and Shepherd, I.T. (2008). Zebrafish sip1a and sip1b are essential for normal axial and neural patterning. Dev. Dyn. *237*, 1060–1069.

Delfino-Machín, M., Madelaine, R., Busolin, G., Nikaido, M., Colanesi, S., Camargo-Sosa, K., Law, E.W.P., Toppo, S., Blader, P., Tiso, N., et al. (2017). Sox10 contributes to the balance of fate choice in dorsal root ganglion progenitors. PLoS One *12*, e0172947.

Ding, H.L., Clouthier, D.E., and Artinger, K.B. (2013). Redundant roles of PRDM family members in zebrafish craniofacial development. Dev. Dyn. *242*, 67–79.

Le Douarin, N., and Kalcheim, C. (1999). The Neural Crest (Cambridge University Press).

Le Douarin, N.M., and Teillet, M.A.M. (1974). Experimental analysis of the migration and differentiation of neuroblasts of the autonomic nervous system and of neurectodermal mesenchymal derivatives, using a biological cell marking technique. Dev. Biol. *41*, 162–184.

Du, J., Miller, A.J., Widlund, H.R., Horstmann, M.A., Ramaswamy, S., and Fisher, D.E. (2003). MLANA/MART1 and SILV/PMEL17/GP100 are transcriptionally regulated by MITF in melanocytes and melanoma. Am. J. Pathol. *163*, 333–343.

Dutton, K.A., Pauliny, A., Lopes, S.S., Elworthy, S., Carney, T.J., Rauch, J., Geisler, R., Haffter, P., and Kelsh, R.N. (2001). Zebrafish Colourless Encodes sox10 and Specifies Non-Ectomesenchymal Neural Crest Fates. Development *128*, 4113–4125.

Elworthy, S., Pinto, J.P., Pettifer, A., Cancela, M.L., and Kelsh, R.N. (2005). Phox2b function in the enteric nervous system is conserved in zebrafish and is sox10-dependent. Mech. Dev. *122*, 659–669.

Epstein, M.L., Mikawa, T., Brown, A.M.C., and McFarlin, D.R. (1994). Mapping the origin of the avian enteric nervous system with a retroviral marker. Dev. Dyn. *201*, 236–244.

Escot, S., Blavet, C., Faure, E., Zaffran, S., Duband, J.L., and Fournier-Thibault, C. (2016). Disruption of CXCR4 signaling in pharyngeal neural crest cells causes DiGeorge syndrome-like malformations. Development *143*, 582–588.

Farnsworth, D.R., Saunders, L.M., and Miller, A.C. (2020). A single-cell transcriptome atlas for zebrafish development. Dev. Biol. *459*, 100–108.

Feregrino, C., Sacher, F., Parnas, O., and Tschopp, P. (2019). A single-cell transcriptomic atlas of the developing chicken limb. BMC Genomics *20*, 401.

Furness, J.B., Jones, C., Nurgali, K., and Clerc, N. (2004). Intrinsic primary afferent neurons and nerve circuits within the intestine. Prog. Neurobiol. *72*, 143–164.

Gandhi, S., Ezin, M., and Bronner, M.E. (2020). Reprogramming Axial Level Identity to Rescue Neural-Crest-Related Congenital Heart Defects. Dev. Cell *53*, 300-315.e4.

Ganz, J. (2018). Gut feelings: Studying enteric nervous system development, function, and disease in the zebrafish model system. Dev. Dyn. *247*, 268–278.

Gaudet, P., Livstone, M.S., Lewis, S.E., and Thomas, P.D. (2011). Phylogenetic-based propagation of functional annotations within the Gene Ontology consortium. Brief. Bioinform. *12*, 449–462.

Gou, Y., Guo, J., Maulding, K., and Riley, B.B. (2018). sox2 and sox3 cooperate to regulate otic/epibranchial placode induction in zebrafish. Dev. Biol. *435*, 84–95.

Graham, A., Begbie, J., and McGonnell, I. (2004). Significance of the Cranial Neural Crest. Dev. Dyn. *229*, 5–13.

Green, S.A., Simoes-costa, M., Bronner, M.E., and Engineering, B. (2016). Evolution of vertebrates: a view from the crest. Nature *520*, 474–482.

Hall, B.K., and Hörstadius, S. (1988). The Neural Crest (London, New York, Tokyo, Toronto: Oxford University Press).

Hans, S., Irmscher, A., and Brand, M. (2013). Zebrafish Foxi1 provides a neuronal ground state during inner ear induction preceding the Dlx3b/4b-regulated sensory lineage. Development *140*, 1936–1945.

Hao, M.M., and Young, H.M. (2009). Development of enteric neuron diversity. J. Cell. Mol. Med. *13*, 1193–1210.

Harrison, C., Wabbersen, T., and Shepherd, I.T. (2014). In vivo visualization of the development of the enteric nervous system using a Tg(-8.3bphox2b: Kaede) transgenic zebrafish. Genesis *52*, 985–990.

Heanue, T.A., and Pachnis, V. (2008). Ret isoform function and marker gene expression in the enteric nervous system is conserved across diverse vertebrate species. Mech. Dev. *125*, 687–699.

Heanue, T.A., Shepherd, I.T., and Burns, A.J. (2016). Enteric nervous system development in avian and zebrafish models. Dev. Biol. *417*, 129–138.

Heffer, A., Marquart, G.D., Aquilina-Beck, A., Saleem, N., Burgess, H.A., and Dawid, I.B. (2017). Generation and characterization of Kctd15 mutations in zebrafish. PLoS One *12*, e0189162.

Higdon, C.W., Mitra, R.D., and Johnson, S.L. (2013). Gene Expression Analysis of Zebrafish Melanocytes, Iridophores, and Retinal Pigmented Epithelium Reveals Indicators of Biological Function and Developmental Origin. PLoS One *8*, e67801.

Holmqvist, B., Ellingsen, B., Forsell, J., Zhdanova, I., and Alm, P. (2004). The early ontogeny of neuronal nitric oxide synthase systems in the zebrafish. J. Exp. Biol. *207*, 923–935.

Hong, E., Santhakumar, K., Akitake, C.A., Ahn, S.J., Thisse, C., Thisse, B., Wyart, C., Mangin, J.M., and Halpern, M.E. (2013). Cholinergic left-right asymmetry in the habenulo-interpeduncular pathway. Proc. Natl. Acad. Sci. U. S. A. *110*, 21171–21176.

Hong, S.K., Tsang, M., and Dawid, I.B. (2008). The Mych gene is required for neural crest survival during zebrafish development. PLoS One *3*, e2029.

Howe, K., Clark, M.D., Torroja, C.F., Torrance, J., Berthelot, C., Muffato, M., Collins, J.E., Humphray, S., McLaren, K., Matthews, L., et al. (2013). The zebrafish reference genome sequence and its relationship to the human genome. Nature *496*, 498–503.

Huang, V., Butler, A.A., and Lubin, F.D. (2019). Telencephalon transcriptome analysis of chronically stressed adult zebrafish. Sci. Rep. *9*, 1379.

Hutchins, E.J., Kunttas, E., Piacentino, M.L., Howard, A.G.A., Bronner, M.E., and Uribe, R.A. (2018). Migration and diversification of the vagal neural crest. Dev. Biol. *444*, S98–S109.

Janssens, E., Gaublomme, D., de Groef, L., Darras, V.M., Arckens, L., Delorme, N., Claes, F., van Hove, I., and Moons, L. (2013). Matrix Metalloproteinase 14 in the Zebrafish: An Eye on Retinal and Retinotectal Development. PLoS One *8*, e52915.

Jarinova, O., Hatch, G., Poitras, L., Prudhomme, C., Grzyb, M., Aubin, J., Bérubé-Simard, F.-A., Jeannotte, L., and Ekker, M. (2008). Functional resolution of duplicated hoxb5 genes in teleosts. Development *135*, 3543–3553.

Jowett, T., and Lettice, L. (1994). Whole-mount in situ hybridizations on zebrafish embryos using a mixture of digoxigenin- and fluorescein- labelled probes. Trends Genet. *10*, 73–74.

Kague, E., Gallagher, M., Burke, S., Parsons, M., Franz-Odendaal, T., and Fisher, S. (2012). Skeletogenic Fate of Zebrafish Cranial and Trunk Neural Crest. PLoS One *7*, e47394.

Kam, M.K.M., and Lui, V.C.H. (2015). Roles of Hoxb5 in the development of vagal and trunk neural crest cells. Dev. Growth Differ. *57*, 158–168.

Kam, M.K.M., Cheung, M.C.H., Zhu, J.J., Cheng, W.W.C., Sat, E.W.Y., Tam, P.K.H., and Lui, V.C.H. (2014). Perturbation of Hoxb5 signaling in vagal and trunk neural crest cells causes apoptosis and neurocristopathies in mice. Cell Death Differ. *21*, 278–289.

Karlsson, J., Von Hofsten, J., and Olsson, P.E. (2001). Generating transparent zebrafish: A refined method to improve detection of gene expression during embryonic development. Mar. Biotechnol. *3*, 522–527.

Kelsh, R.N. (2004). Genetics and evolution of pigment patterns in fish. Pigment Cell Res. *17*, 326–336.

Kelsh, R.N., and Eisen, J.S. (2000). The zebrafish colourless gene regulates development of non-ectomesenchymal neural crest derivatives. Development *127*, 515–525.

Kimmel, C.B., Ballard, W.W., Kimmel, S.R., Ullmann, B., and Schilling, T.F. (1995). Stages of embryonic development of the zebrafish. Dev. Dyn. *203*, 253–310.

Knight, R.D., Nair, S., Nelson, S.S., Afshar, A., Javidan, Y., Geisler, R., Rauch, G.J., and Schilling, T.F. (2003). Lockjaw encodes a zebrafish tfap2a required for early neural crest development. Development *130*, 5755–5768.

Kuo, B.R., and Erickson, C.A. (2011). Vagal neural crest cell migratory behavior: A transition between the cranial and trunk crest. Dev. Dyn. *240*, 2084–2100.

Kwak, J., Park, O.K., Jung, Y.J., Hwang, B.J., Kwon, S.H., and Kee, Y. (2013). Live image profiling of neural crest lineages in zebrafish transgenic lines. Mol. Cells *35*, 255–260.

Lasrado, R., Boesmans, W., Kleinjung, J., Pin, C., Bell, D., Bhaw, L., McCallum, S., Zong, H., Luo, L., Clevers, H., et al. (2017). Lineage-dependent Spatial and Functional Organization of the Mammalian Enteric Nervous System. Science (80-.). *356*, 722–726.

Leigh, N.R., Schupp, M.O., Li, K., Padmanabhan, V., Gastonguay, A., Wang, L., Chun, C.Z., Wilkinson, G.A., and Ramchandran, R. (2013). Mmp17b Is Essential for Proper Neural Crest Cell Migration In Vivo. PLoS One *8*, e76484.

Le Lievre, C.S., and Le Douarin, N.M. (1975). Mesenchymal derivatives of the neural crest: analysis of chimaeric quail and chick embryos. J. Embryol. Exp. Morphol. *34*, 125–154.

Ling, I.T.C., and Sauka-Spengler, T. (2019). Early chromatin shaping predetermines multipotent vagal neural crest into neural, neuronal and mesenchymal lineages. Nat. Cell Biol. *21*, 1504–1517.

Lister, J.A. (2002). Development of pigment cells in the zebrafish embryo. Microsc. Res. Tech. *58*, 435–441.

Lister, J.A., Robertson, C.P., Lepage, T., Johnson, S.L., and Raible, D.W. (1999). Nacre Encodes a Zebrafish Microphthalmia-Related Protein That Regulates Neural-Crest-Derived Pigment Cell Fate. Development *126*, 3757–3767.

Lister, J.A., Lane, B.M., Nguyen, A., and Lunney, K. (2011). Embryonic expression of zebrafish MiT family genes Tfe3b, Tfeb, and Tfec. Dev. Dyn. *240*, 2529–2538.

Liu, R.-Z., Sharma, M.K., Sun, Q., Thisse, C., Thisse, B., Denovan-Wright, E.M., and Wright, J.M. (2005). Retention of the Duplicated Cellular Retinoic Acid-Binding Protein 1 Genes (crabp1a and

crabp1b) in the Zebrafish Genome by Subfunctionalization of Tissue-Specific Expression. FEBS J. *272*, 3561–3571.

Lu, J.-K., Tsai, T.-C., Lee, H., Hsia, K., Lin, C.-H., and Lu, J.-H. (2019). Pectoral Fin Anomalies in tbx5a Knockdown Zebrafish Embryos Related to the Cascade Effect of N-Cadherin and Extracellular Matrix Formation. J. Dev. Biol. *7*, 15.

Ludwig, A., Rehberg, S., and Wegner, M. (2004). Melanocyte-specific expression of dopachrome tautomerase is dependent on synergistic gene activation by the Sox10 and Mitf transcription factors. FEBS Lett. *556*, 236–244.

Luo, R., An, M., Arduini, B.L., and Henion, P.D. (2001). Specific pan-neural crest expression of zebrafish crestin throughout embryonic development. Dev. Dyn. *220*, 169–174.

Martik, M.L., and Bronner, M.E. (2017). Regulatory Logic Underlying Diversification of the Neural Crest. Trends Genet. *33*, 715–727.

Matini, P., Manneschi, L.I., Mayer, B., and Faussone-Pellegrini, M.S. (1995). Nitric oxide producing neurons in the human colon: an immunohistochemical and histoenzymatical study. Neurosci. Lett. *193*, 17–20.

McGraw, H.F., Nechiporuk, A., and Raible, D.W. (2008). Zebrafish Dorsal Root Ganglia Neural Precursor Cells Adopt a Glial Fate in the Absence of neurogenin1. J. Neurosci. *28*, 12558–12569.

Mcinnes, L., Healy, J., and Melville, J. (2018). UMAP: Uniform Manifold Approximation and Projection for Dimension Reduction. ArXiv 1802.03426v2.

Memic, F., Knoflach, V., Morarach, K., Sadler, R., Laranjeira, C., Hjerling-Leffler, J., Sundström, E., Pachnis, V., and Marklund, U. (2018). Transcription and Signaling Regulators in Developing Neuronal Subtypes of Mouse and Human Enteric Nervous System. Gastroenterology *154*, 624–636.

Minchin, J.E.N., and Hughes, S.M. (2008). Sequential actions of Pax3 and Pax7 drive xanthophore development in zebrafish neural crest. Dev. Biol. *317*, 508–522.

Minoux, M., and Rijli, F.M. (2010). Molecular mechanisms of cranial neural crest cell migration and patterning in craniofacial development. Development *137*, 2605–2621.

Morarach, K., Mikhailova, A., Knoflach, V., Memic, F., Kumar, R., Li, W., Ernfors, P., and Marklund, U. (2020). Diversification of molecularly defined myenteric neuron classes revealed by single cell RNA-sequencing. BioRxiv 2020.03.02.955757.

Nagy, N., and Goldstein, A.M. (2017). Enteric Nervous System Development: A Crest Cell's Journey From Neural Tube to Colon. Semin. Cell Dev. Biol. *66*, 94–106.

Nakamura, T., Gehrke, A.R., Lemberg, J., Szymaszek, J., and Shubin, N.H. (2016). Digits and fin rays share common developmental histories. Nature *537*, 225–228.

Nord, H., Dennhag, N., Muck, J., and Von Hofsten, J. (2016). Pax7 is required for establishment of the xanthophore lineage in zebrafish embryos. Mol. Biol. Cell *27*, 1853–1862.

Olden, T., Akhatar, T., Beckman, S.A., and Wallace, K.N. (2008). Differentiation of the Zebrafish Enteric Nervous System and Intestinal Smooth Muscle. Genesis *46*, 484–498.

van Otterloo, E., Li, W., Garnett, A., Cattell, M., Medeiros, D.M., and Cornell, R.A. (2012). Novel Tfap2-mediated control of soxE expression facilitated the evolutionary emergence of the neural crest. Development *139*, 720–730.

Parichy, D.M., Ransom, D.G., Paw, B., Zon, L.I., and Johnson, S.L. (2000). An Orthologue of the Kit-Related Gene Fms Is Required for Development of Neural Crest-Derived Xanthophores and a Subpopulation of Adult Melanocytes in the Zebrafish, Danio Rerio. Development *127*, 3031–3044.

Parichy, D.M., Elizondo, M.R., Mills, M.G., Gordon, T.N., and Engeszer, R.E. (2009). Normal table of postembryonic zebrafish development: Staging by externally visible anatomy of the living fish. Dev. Dyn. *238*, 2975–3015.

Parker, H.J., Pushel, I., and Krumlauf, R. (2018). Coupling the roles of Hox genes to regulatory networks patterning cranial neural crest. Dev. Biol. *444*, S67–S78.

Parker, H.J., De Kumar, B., Green, S.A., Prummel, K.D., Hess, C., Kaufman, C.K., Mosimann, C., Wiedemann, L.M., Bronner, M.E., and Krumlauf, R. (2019). A Hox-TALE regulatory circuit for neural crest patterning is conserved across vertebrates. Nat. Commun. *10*, 1182.

Petratou, K., Subkhankulova, T., Lister, J.A., Rocco, A., Schwetlick, H., and Kelsh, R.N. (2018). A Systems Biology Approach Uncovers the Core Gene Regulatory Network Governing Iridophore Fate Choice From the Neural Crest. PLOS Genet. *14*, e1007402.

Petratou, K., Spencer, S.A., Kelsh, R.N., and Lister, J.A. (2019). The MITF paralog tfec is required in neural crest development for fate specification of the iridophore lineage from a multipotent pigment cell progenitor. BioRxiv 862011.

Poon, K.L., Richardson, M., Lam, C.S., Khoo, H.E., and Korzh, V. (2003). Expression pattern of neuronal nitric acid oxide synthase in embryonic zebrafish. Gene Expr. Patterns *3*, 463–466.

Qu, Z.D., Thacker, M., Castelucci, P., Bagyánszki, M., Epstein, M.L., and Furness, J.B. (2008). Immunohistochemical analysis of neuron types in the mouse small intestine. Cell Tissue Res. *334*, 147–161.

Quigley, I.K., and Parichy, D.M. (2002). Pigment pattern formation in zebrafish: A model for developmental genetics and the evolution of form. Microsc. Res. Tech. *58*, 442–455.

R Core Team (2020). R. R A Lang. Environ. Stat. Comput. R Found. Stat. Comput.

Rajan, S.G., Gallik, K.L., Monaghan, J.R., Uribe, R.A., Bronner, M.E., and Saxena, A. (2018). Tracking neural crest cell cycle progression in vivo. Genesis *56*, e23214.

Rao, M., and Gershon, M.D. (2018). Enteric nervous system development: what could possibly go wrong? Nat. Rev. Neurosci. *19*, 552–565.

Reedy, M. V., Faraco, C.D., and Erickson, C.A. (1998). Specification and migration of melanoblasts at the vagal level and in hyperpigmented silkie chickens. Dev. Dyn. *213*, 476–485.

Rocha, M., Singh, N., Ahsan, K., Beiriger, A., and Prince, V.E. (2020). Neural crest development: insights from the zebrafish. Dev. Dyn. *249*, 88–111.

Rodrigues, F.S.L.M., Doughton, G., Yang, B., and Kelsh, R.N. (2012). A novel transgenic line using the Cre-lox system to allow permanent lineage-labeling of the zebrafish neural crest. Genesis *50*, 750–757.

Rueden, C.T., Schindelin, J., Hiner, M.C., Dezonia, B.E., Walter, A.E., Arena, E.T., and Eliceiri, K.W. (2017). ImageJ2: ImageJ for the next generation of scientific image data. BMC Bioinformatics *18*, 529.

Ruzicka, L., Howe, D.G., Ramachandran, S., Toro, S., Van Slyke, C.E., Bradford, Y.M., Eagle, A., Fashena, D., Frazer, K., Kalita, P., et al. (2019). The Zebrafish Information Network: new support for non-coding genes, richer Gene Ontology annotations and the Alliance of Genome Resources. Nucleic Acids Res. *47*, D867-873.

Satija, R., Farrell, J.A., Gennert, D., Schier, A.F., and Regev, A. (2015). Spatial reconstruction of single-cell gene expression data. Nat. Biotechnol. *33*, 495–502.

Sauka-Spengler, T., and Bronner-Fraser, M. (2008). A gene regulatory network orchestrates neural crest formation. Nat. Rev. Mol. Cell Biol. *9*, 577–568.

Saunders, L.M., Mishra, A.K., Aman, A.J., Lewis, V.M., Toomey, M.B., Packer, J.S., Qiu, X., McFaline-Figueroa, J.L., Corbo, J.C., Trapnell, C., et al. (2019). Thyroid hormone regulates distinct paths to maturation in pigment cell lineages. Elife *8*, e45181.

Schindelin, J., Arganda-Carreras, I., Frise, E., Kaynig, V., Longair, M., Pietzsch, T., Preibisch, S., Rueden, C., Saalfeld, S., Schmid, B., et al. (2012). Fiji: an open-source platform for biological-image analysis. Nat. Methods *9*, 676–682.

Schneider, C.A., Rasband, W.S., and Eliceiri, K.W. (2012). NIH Image to ImageJ: 25 years of image analysis. Nat. Methods *9*, 671–675.

Shepherd, I.T., Pietsch, J., Elworthy, S., Kelsh, R.N., and Raible, D.W. (2004). Roles for GFRα1 receptors in zebrafish enteric nervous system development. Development *131*, 241–249.

Simoes-Costa, M., and Bronner, M.E. (2016). Reprogramming of avian neural crest axial identity and cell fate. Science (80-.). *352*, 1570–1573.

Simões-Costa, M., Tan-Cabugao, J., Antoshechkin, I., Sauka-Spengler, T., and Bronner, M.E. (2014). Transcriptome analysis reveals novel players in the cranial neural crest gene regulatory network. Genome Res. *24*, 281–290.

Singleman, C., and Holtzman, N.G. (2014). Growth and maturation in the zebrafish, Danio Rerio: A staging tool for teaching and research. Zebrafish *11*, 396–406.

Soldatov, R., Kaucka, M., Kastriti, M.E., Petersen, J., Chontorotzea, T., Englmaier, L., Akkuratova, N., Yang, Y., Häring, M., Dyachuk, V., et al. (2019). Spatio-temporal structure of cell fate decisions in murine neural crest. Science (80-.). *364*, eaas9536.

Sperber, S.M., and Dawid, I.B. (2008). barx1 is necessary for ectomesenchyme proliferation and osteochondroprogenitor condensation in the zebrafish pharyngeal arches. Dev. Biol. *321*, 101–110.

Sperber, S.M., Saxena, V., Hatch, G., and Ekker, M. (2008). Zebrafish dlx2a Contributes to Hindbrain Neural Crest Survival, Is Necessary for Differentiation of Sensory Ganglia and Functions With dlx1a in Maturation of the Arch Cartilage Elements. Dev. Biol. *314*, 59–70.

Stewart, R.A., Arduini, B.L., Berghmans, S., George, R.E., Kanki, J.P., Henion, P.D., and Look, A.T. (2006). Zebrafish foxd3 Is Selectively Required for Neural Crest Specification, Migration and Survival. Dev. Biol. *292*, 174–188.

Strausberg, R.L., Feingold, E.A., Grouse, L.H., Derge, J.G., Klausner, R.D., Collins, F.S., Wagner, L., Shenmen, C.M., Schuler, G.D., Altschul, S.F., et al. (2002). Generation and initial analysis of more than 15,000 full-length human and mouse cDNA sequences. Proc. Natl. Acad. Sci. U. S. A. *99*, 16899–16903.

Stuart, T., Butler, A., Hoffman, P., Hafemeister, C., Papalexi, E., Mauck, W.M., Hao, Y., Stoeckius, M., Smibert, P., and Satija, R. (2019). Comprehensive Integration of Single-Cell Data. Cell *177*, 1888-1902.e21.

Tambalo, M., Mitter, R., and Wilkinson, D.G. (2020). A single cell transcriptome atlas of the developing zebrafish hindbrain. Dev. *147*, dev184143.

Taylor, C.R., Montagne, W.A., Eisen, J.S., and Ganz, J. (2016). Molecular fingerprinting delineates progenitor populations in the developing zebrafish enteric nervous system. Dev. Dyn. *245*, 1081–1096.

Theodore, L.N., Hagedorn, E.J., Cortes, M., Natsuhara, K., Liu, S.Y., Perlin, J.R., Yang, S., Daily, M.L., Zon, L.I., and North, T.E. (2017). Distinct Roles for Matrix Metalloproteinases 2 and 9 in Embryonic Hematopoietic Stem Cell Emergence, Migration, and Niche Colonization. Stem Cell Reports *8*, 1226–1241.

Theveneau, E., and Mayor, R. (2012). Neural crest delamination and migration: From epithelium-to-mesenchyme transition to collective cell migration. Dev. Biol. *366*, 34–54.

Thisse, B., and Thisse, C. (2004). Fast Release Clones: A High Throughput Expression Analysis. ZFIN Direct Data Submission. (http://zfin.org).

Thisse, C., and Thisse, B. (2005). High Throughput Expression Analysis of ZF-Models Consortium Clones. ZFIN Direct Data Submission. http://zfin.org.

Thisse, B., Pflumio, S., Fürthauer, M., Loppin, B., Heyer, V., Degrave, A., Woehl, R., Lux, A., Steffan, T., Charbonnier, X.., et al. (2001). Expression of the zebrafish genome during embryogenesis. ZFIN Direct Data Submission. (http://zfin.org).

Uribe, R.A., and Bronner, M.E. (2015). Meis3 is required for neural crest invasion of the gut during zebrafish enteric nervous system development. Mol. Biol. Cell *26*, 3728–3740.

Uyttebroek, L., Shepherd, I.T., Harrisson, F., Hubens, G., Blust, R., Timmermans, J.P., and van Nassauw, L. (2010). Neurochemical coding of enteric neurons in adult and embryonic zebrafish (Danio rerio). J. Comp. Neurol. *518*, 4419–4438.

Vega-Lopez, G.A., Cerrizuela, S., and Aybar, M.J. (2017). Trunk neural crest cells: formation, migration and beyond. Int. J. Dev. Biol. *61*, 5–15.

Veraksa, A., Del Campo, M., and McGinnis, W. (2000). Developmental patterning genes and their conserved functions: From model organisms to humans. Mol. Genet. Metab. *69*, 85–100.

Wagner, D.E., Weinreb, C., Collins, Z.M., Briggs, J.A., Megason, S.G., and Klein, A.M. (2018). Single-cell mapping of gene expression landscapes and lineage in the zebrafish embryo. Science (80-.). *360*, 981–987.

Wang, H.H., Chen, H.S., Li, H.B., Zhang, H., Mei, L.Y., He, C.F., Wang, X.W., Men, M.C., Jiang, L., Liao, X. Bin, et al. (2014). Identification and functional analysis of a novel mutation in the SOX10 gene associated with Waardenburg syndrome type IV. Gene *538*, 36–41.

Wang, W. Der, Melville, D.B., Montero-Balaguer, M., Hatzopoulos, A.K., and Knapik, E.W. (2011). Tfap2a and Foxd3 regulate early steps in the development of the neural crest progenitor population. Dev. Biol. *360*, 173–185.

Williams, A.L., and Bohnsack, B.L. (2015). Neural crest derivatives in ocular development: Discerning the eye of the storm. Birth Defects Res. Part C Embryo Today Rev. *105*, 87–95.

Williams, R.M., Candido-Ferreira, I., Repapi, E., Gavriouchkina, D., Senanayake, U., Ling, I.T.C., Telenius, J., Taylor, S., Hughes, J., and Sauka-Spengler, T. (2019). Reconstruction of the Global Neural Crest Gene Regulatory Network In Vivo. Dev. Cell *51*, 522-576.e7.

Wilson, Y.M., Richards, K.L., Ford-Perriss, M.L., Panthier, J.J., and Murphy, M. (2004). Neural crest cell lineage segregation in the mouse neural tube. Development *131*, 6153–6162.

Yelon, D., Brauch, T., Halpern, M.E., Ruvisnsky, I., Ho, R.K., Silver, L.M., and Stainier, D.Y.R. (2000). The bHLH transcription factor Hand2 plays parallel roles in zebrafish heart and pectoral fin development. Development *127*, 2573–2582.

Yntema, C.L., and Hammond, W.S. (1954). The origin of intrinsic ganglia of trunk viscera from vagal neural crest in the chick embryo. J. Comp. Neurol. *101*, 515–541.

Zheng, G.X.Y., Terry, J.M., Belgrader, P., Ryvkin, P., Bent, Z.W., Wilson, R., Ziraldo, S.B., Wheeler, T.D., Mcdermott, G.P., Zhu, J., et al. (2017). Massively parallel digital transcriptional profiling of single cells. Nat. Commun. *8*, 14049.

Zoli, M. (2000). Distribution of Cholinergic Neurons in the Mammalian Brain with Special Reference to their Relationship with Neuronal Nicotinic Acetylcholine Receptors. In Neuronal Nicotinic Receptors. Handbook of Experimental Pharmacology, F. Clementi, D. Fornasari, and C. Gotti, eds. (Berlin, Heidelberg: Springer), pp. 13–30.

Figure Legends

Figure 1. Single-Cell profiling strategy from the posterior zebrafish during the embryonic to larval stage transition.

(A) Confocal image of *sox10*:GFP^{+} embryo at 48 hpf. Hb: Hindbrain; Sc: Spinal cord. A: Anterior, P: Posterior, D: Dorsal, V: Ventral. Scale bar: 50 μM

(B) Cartoon illustrations of a zebrafish embryo at 48-50 hpf and an early larval fish at 68-70 hpf depicted laterally to summarize the dissection workflow used to collect posterior *sox10*:GFP^{+} cells.

(C) Schematic of the 10X Genomics Chromium and data analysis pipeline.

Figure 2. Cell population composition of posterior *sox10*:GFP^{+} embryonic cells at 48-50 hpf.

(A) Heatmap summarizing the top 10 genes significantly expressed in each cluster, for Clusters 0-18. Relative expression levels within each cluster is summarized within the color key, where yellow to magenta color indicates high to low gene expression levels. **(B)** A tSNE plot reveals the arrangement of Clusters 0-18.

(C) A heatmap summarizing the Major Cell Types identified among *sox10*:GFP^{+} cells. Relative expression levels within each Major Cell Type cluster is summarized within the color key, where yellow to magenta color indicates high to low gene expression levels

(D) A tSNE plot showing where the Major Cell Types identified among *sox10*:GFP^{+} cells arrange in the 48-50 hpf data set.

(E) tSNE plots depicting the Major Cell Type classification representative gene marker for each major cell type category. Relative expression levels are summarized within the color keys, where color intensity is proportional to expression level of each gene depicted.

(F) Dot plot of the identifying gene markers for each Major Cell Type classification in the 48-50 hpf data set. Dot size depicts the cell percentage for each marker within the data set and the color summarizes the average expression levels for each gene.

Figure 3. Cell population composition of posterior *sox10*:GFP^{+} larval cells at 68-70 hpf.

(A) Heatmap summarizing the top 10 genes significantly expressed in each cluster, for Clusters 0-22. Relative expression levels within each cluster is summarized within the color key, where yellow to magenta color indicates high to low gene expression levels. **(B)** A tSNE plot reveals the arrangement of Clusters 0-22.

(C) A heatmap summarizing the Major Cell Types identified among *sox10*:GFP^{+} cells. Relative expression levels within each Major Cell Type cluster is summarized within the color key, where yellow to magenta color indicates high to low gene expression levels

(D) A tSNE plot showing where the Major Cell Types identified among *sox10*:GFP^{+} cells arrange in the 68-70 hpf data set.

(E) tSNE plots depicting the Major Cell Type classification representative gene marker for each major cell type category. Relative expression levels are summarized within the color keys, where color intensity is proportional to expression level of each gene depicted.

(F) Dot plot of the identifying gene markers for each Major Cell Type classification in the 68-70 hpf data set. Dot size depicts the cell percentage for each marker within the data set and the color summarizes the average expression levels for each gene.

Figure 4. Distinct pigment cell populations are present during embryonic to larval transition.

(A) Cartoon schematic depicting the model for neural crest delineation into pigment cell lineages and the genes that were used to identify each pigment cell population.

(B) Dot plot identifying melanophore markers within the 48-50 hpf data set. Dot size depicts the cell percentage for each marker within the data set and the color summarizes the average expression levels for each gene.

(C) tSNE plots depicting melanophore signature in the 48-50 hpf data set. Relative expression levels are summarized within the color keys, where color intensity is proportional to expression level of each gene depicted.

(D) Dot plot showing distinct pigment chromatophore markers within the 68-70 hpf data set. Dot size depicts the cell percentage for each marker within the data set and the color summarizes the average expression levels for each gene. M: melanophore markers; X: xanthophore markers; I: iridophore markers.

(E-G) tSNE plots revealing the location of melanophores **(E)**, xanthophores **(F)**, and iridophores **(G)** in the 68-70 hpf data set. Relative expression levels are summarized within the color keys, where color intensity is proportional to expression level of each gene depicted.

(H) HCR against *mitfa* and *tfec* at 48-50 hpf reveals *mitfa*$^{+}$ melanophores (white arrowhead) and *mitfa*$^{+}$/*tfec*$^{+}$ pigment progenitors (red arrowhead). Cropped panels show individual fluorescent channels.

(I) HCR against *mitfa* and *tfec* at 68-70 hpf presents *mitfa*$^{+}$ melanophores (white arrowhead), *tfec*$^{+}$ iridophores (blue arrowhead), and *mitfa*$^{+}$/*tfec*$^{+}$ pigment progenitors (red arrowhead). Cropped panels show individual fluorescent channels.

(J) HCR against *mitfa* and *xdh* at 68-70 hpf shows *mitfa*$^{+}$/*xdh*$^{+}$ xanthophores (orange arrowhead). Cropped panels show individual fluorescent channels.

Scale bar in H-J: 50 μm.

Figure 5. Global analysis of mesenchyme cell signatures.

(A,B) A heatmap of signature Mesenchyme identity genes within the Major Cell Type classified cells at 48-50 and 68-70 hpf, respectively. Relative expression levels within each cluster is

summarized within the color key, where red to blue color indicates high to low gene expression levels.

(C) A Cluster Tree depicting the relationship between general and chondrogenic mesenchyme cellular subtypes.

(D) Violin plots summarizing the expression levels for select Mesenchyme identity markers within individual clusters at the 48-50 and 68-70 hpf time points, respectively. Data points depicted in each cluster represent single cells expressing each gene shown.

(E,L) tSNE plots depicting the expression of *prrx1b*, *barx1* and *twist1a* in the 48-50 and 68-70 hpf data sets, respectively. Relative expression levels are summarized within the color keys, where color intensity is proportional to expression level of each gene depicted.

(F-K) Whole Mount HCR analysis reveals the spatiotemporal expression of *prrx1b* **(F)**, *twist1a* **(G)**, *sox10:*GFP **(H)**, *barx1* **(J)** in 48 hpf embryos. **(I)** A merge of *barx1*, *prrx1b* and *twist1a* is shown. **(K)** A merge of *barx1*, *prrx1b*, *twist1a* and *sox10*:GFP is shown. White arrowheads denote expression in posterior pharyngeal arch, while yellow arrowheads highlight fin bud expression.

(M-R) Wholemount HCR analysis reveals the spatiotemporal expression of *prrx1b* **(M)**, *twist1a* **(N)**, *sox10:*GFP **(O)**, *barx1* **(Q)** in 68 hpf embryos. **(P)** A merge of *barx1*, *prrx1b* and *twist1a* is shown. **(R)** A merge of *barx1*, *prrx1b*, *twist1a* and *sox10*:GFP is shown. White arrowheads denote expression in posterior pharyngeal arch, while yellow arrowheads highlight fin bud expression.

Ot: otic; Fb: Fin bud. Scale bar: 100 μm.

Figure 6. **Enteric neural crest cells are present among posterior *sox10*:GFP^{+} embryonic cells at 48-50 hpf.**

(A) tSNE feature plots reveal expression of core neural crest cell markers *sox10*, *foxd3*, *crestin* and *tfap2a* mapping to the neural crest cell cluster (red arrow).

(B) tSNE feature plots depict expression of the enteric neural crest cell markers *phox2bb*, *ret*, *ngfrb* and *gfra1a* within the neural crest cell cluster (red arrow).

Relative expression levels are summarized within the color keys in **(A)** and **(B)**, where color intensity is proportional to expression level of each gene depicted.

(C) A heatmap reveals expression levels of enteric neural crest cell markers across the 8 major cell populations captured in the 48-50 hpf data set (color key denotes cells types represented in color bar on top of heatmap). Neural crest cell cluster highlighted in black rectangle. Relative expression levels within each Major Cell Type cluster is summarized within the color key, where yellow to magenta color indicates high to low gene expression levels.

(D) Dot plot of expanded list of neural crest (green line) and enteric neural crest (purple line) cell markers across each major cell type within 48-50 hpf data set. Dot size depicts the cell percentage for each marker within the data set and the color summarizes the average expression levels for each gene.

(E, F) Wholemount HCR analysis of 48 hpf embryos reveals co-expression of enteric neural crest cell markers within the developing Gut (dashed outline). Top panels depict merged images of color channels for each HCR probe. Lower panels represent grey-scale images of each separated channel corresponding to the magnified region of foregut (grey rectangle). Arrows depict regions where all markers are found to be co-expressed. Hb: Hindbrain, Sc: Spinal cord, pLLg: posterior Lateral Line ganglia, LL: Lateral Line. A: Anterior, P: Posterior, D: Dorsal, V: Ventral. Scale bar: 50 μM.

Figure 7. **Differentiating enteric neurons captured during key transitional stage of subtype diversification within 68-70 hpf *sox10*:GFP^{+} larval cells.**

(A) tSNE feature plots reveal expression levels of enteric neuron markers *elavl3, phox2bb, gfra1a, nos1*, *vipb* and *ret*, within a common region of a neuronal cluster (red arrow). Relative expression levels are summarized within the color keys, where color intensity is proportional to expression level of each gene depicted.

(B) Dot plot depicts expression levels of pan-neuronal and enteric neuron specific markers across individual clusters generated within the original 68-70 hpf tSNE. Pan-neuronal markers found throughout clusters 5 and 12, with enteric neuron markers most prominently expressed within cluster 12. Dot size depicts the cell percentage for each marker within the data set and the color summarizes the average expression levels for each gene.

(C) Wholemount HCR analysis depicts differentiating enteric neurons within the foregut region at 69 hpf co-expressing *nos1, phox2bb, vipb, and elavl3* (yellow arrow). Anterior: Left, Posterior: Right. Scale bar: 50 μM.

(D) tSNE plot reveals 5 distinct clusters following the subset analysis and re-clustering of clusters 5 and 12 from the 68-70 hpf data set.

(E) Dot plot depicts expression levels of enteric neuron markers across resulting sub-clusters. Each marker was expressed at low levels in cluster 1 and were found to be expressed at higher levels within cluster 4.

(F) tSNE feature plots further depict the expression of enteric neuron markers by illustrating the levels and localization of expression within the sub-cluster architecture. Feature plots supplement dot plot and demonstrate the prominent expression of enteric neuron markers within cluster 4, which appears to emanate from cluster 1.

(G) Violin and feature plots reveal expression levels of acetylcholine associated and excitatory neuron markers reported to distinguish enteric IPANs. These markers were found in a discrete pocket of cells forming the distal-most region of sub-cluster 4 (red arrow). Violin data points depicted in each cluster represent single cells expressing each gene shown.

(H) Wholemount HCR analysis reveals co-expression of IPAN markers, *pbx3b* and *calb2a,* and inhibitory neurochemical markers, *vipb* and *nos1* (white arrows), within the foregut (dashed white line) at 68 hpf. Vesicular acetylcholine transferase, *slc18a3a* was not observed in tandem with *pbx3b* but was co-expressed with *calb2a, vipb,* and *nos1* (yellow arrow). Scale bar: 50 μM.

(I) Graphical model summarizes expression patterns observed in 68-70 hpf data set and HCR validation. Common enteric neuroblast capable of diverging into subsequent lineages, IPAN, inhibitory neuron, and interneuron through lineage restricted gene expression. *Pbx3b* promotes assumption of IPAN role through loss of *nos1* and *vipb* and begins expressing *calb2a, ache* and *slc18a3a*.

Figure 8. Integrated Atlas of *sox10*:GFP^{+} Cell types spanning the embryonic to larval transition.

(A) Global UMAP embedding demonstrating the clustering of cell types across 48-50 hpf and 68-70 hpf. Cell labels were transferred from the original curation to the new atlas after its creation, allowing for unbiased assessment of cell type organization.

(B) Previously identified mesenchyme clusters form a large discernible cluster marked by *prrx1b*, *twist1a*, *foxc1a*, and *snai1a*, which was separated into both chondrogenic and general mesenchyme, as denoted by its differential expression of *barx1* and *dlx2a*. Importantly, nearly every 48-50 hpf cell type nests with a cluster at 68-70 hpf.

(C) Pigment cells clusters reflect differentiation paths described in Fig. 4A. Melanophores at 48-50 hpf group near to the 68-70 hpf Melanophore cluster, bipotent pigment progenitors bridges both the Iridophores and Melanophores. Xanthophores cluster separately, reflecting their distinct lineage of origin at this developmental window.

(D) Detailed analysis of the larger Neural/Neuronal cluster shows clear progression of cell fates from progenitor to differentiating glia or neuron. We confirm the presence of a clear enteric neuronal population, which is distinct from other subtypes at this data set.

Figure 9. **Description of Hox genes expressed per major cell identity within the Atlas.**

(A) Dot plot shows both the expression (color) as well as percent of cells (size) for each *hox* factor assayed. There are discrete *hox* profiles which discern specific cell types.

(B) *hox* gene expression is ubiquitously detected across the neural, neuronal, mesenchyme, and pigment clusters. The otic epithelium, muscle and unidentified cell clusters all lack strong *hox* expression profiles.

(C-G) Specific exemplary expression profiles shown in the atlas for the cluster types: neural **(C)**, enteric neuronal **(D)**, fin bud mesenchyme **(E)**, and CNS neuron **(F)**. Lastly, the expression of *hoxb7a* showed differential expression across several cell types, including certain pigment and neural cell populations **(G)**.

Figure S1. **Statistics on generation of high quality single cell transcriptomes at 48-50 hpf and 68-70 hpf.**

(A,B) Fluorescence activated cell sorting plots highlighting the GFP^{+} cell population sorted at 48-50 hpf **(A)** and 69-70 hpf **(B)**.

(C) Table of general statistics output as an end result of the sequencing and alignment from the Cell Ranger pipeline. Additional metrics provided were derived from the Seurat R package.

(D,E) Plots showing the feature selection for both the 48-50 hpf **(D)** and 69-70 hpf **(E)** data sets. Cells were selected such that they had fewer than 2500 features to reduce spuriously sorted cells.

(F,G) Top 2000 most variably expressed genes were identified and used for further downstream identification of significant principal components.

(H,I) Most significant principle components (top 20 for both data sets) were selected to be used for subsequent cluster identification and cell embedding in tSNE and UMAP spaces.

Figure S2. Major Cell Type Categories and Cell Cycle Distributions of the scRNA-seq data sets.

(A,B) tSNE plots summarizing the G1, S and G2/M phase cell cycle phase occupancies of the cells in the 48-50 and 68-70 hpf time points, respectively.

(C,E) A tSNE plot depicting the expression of *aurkb*, a G2/M phase marker, within the 48-50 and 68-70 hpf data sets, respectively. Relative expression levels are summarized within the color keys, where color intensity is proportional to expression level of each gene depicted.

(D,F) A tSNE plot depicting the expression of *mcm3*, a S phase marker, within the 48-50 and 68-70 hpf data sets, respectively. Relative expression levels are summarized within the color keys, where color intensity is proportional to expression level of each gene depicted.

(G) Bar graphs summarizing the cell cycle phase occupancies, as a fraction of cells within the total data sets for each time point.

(H) Bar graphs summarizing the Major Cell Type categories, as a fraction of cells within the total data sets for each time point.

(I) Table summarizing the cell cycle genes used to demarcate cell cycle phase occupancy categories within the scRNA-seq data sets.

Figure S3. **Table summarizing the top identify markers used for major Cell type and subtype cellular classifications for each cluster at 48-50 and 68-70 hpf.**

Figure S4. **Identification of otic vesicle, muscle, and central nervous system (CNS) cellular populations**

(A) Panel of tSNE feature plots at 48-50 hpf that identify combinatorial expression of otic vesicle (*otomp, cldna,cldn7b, and epcam),* muscle (*ckmb, actc1b, tnnt3a, and tpma),* or CNS *(slc32a1, gad1b, slc6a5, gata2a)* markers. Cluster of interest denoted by black arrows.

(B) Panel of tSNE feature plots at 68-70 hpf that identify combinatorial expression of otic vesicle markers *(otomp, cldna, cldn7b, and epcam)* or muscle *(ckmb, actc1b, tnnt3a, and tpma).* Cluster of interest denoted by black arrows.

Figure S5. **Identification of fin bud and sensory neuronal progenitor cellular populations**

(A) Panel of tSNE feature plots of sensory neuronal progenitors at 48-50 hpf that show combinatorial expression of *neurod4, neurod1, vim, and ngfrb,* Cluster of interest denoted by black arrows.

(B) Panel of tSNE feature plots of fin bud makers at 48-50 hpf (top) and 68-70 hpf (bottom) that show combinatorial expression of *tbx5a, hand2, hoxd13a,* and *prrx1a.* Cluster of interest denoted by black arrows.

Figure S6. **Enteric neuron subtype diversification gene expression patterns seen in enteric neuron sub-cluster.**

(A) Panel of tSNE feature plots magnified and cropped to focus on progressively differentiating enteric neurons (highlighted by *etv1* expression). Subtype diversification and IPAN emergence depicted via combinatorial gene expression (*etv1, ntng1aa, pbx3b, slc18a3a, calb2a,* and *ache)* localized to the distal tip of sub-cluster 4. Inhibitory neuron markers, *nos1, vip,* and galanin (*galn*) were present within the pocket of diverging enteric subtypes.

Figure S7. **Wholemount *in situ* hybridization of select ENCC, Mesenchyme and Neural markers at 48-50 hpf**.

(A,A') The marker *sox10* is shown along the vagal region and within ENCC along the foregut in (**A'**; highlighted via arrowheads). Scale bar in **A**: 60 μM, in **A'**: 40 μM.

(B, B') Expression of *phox2bb* is shown within the hindbrain-axial level of the embryo, as well as within ENCC within the foregut (**B'**; highlighted via arrowheads). Scale bar in **A**: 60 μM, in **A'**: 40 μM.

(C,D) The mesenchyme markers *mmp2* (**C**, highlighted via arrowheads) and *foxc1a* (**D**; highlighted via arrowheads) are expressed within the posterior pharyngeal arches and the ventral mesenchyme.

(E,F) The neural markers *notch1a* **(E)** and *dla* **(F)** are expressed within the hindbrain and spinal cord (arrowheads). **(F)** *dla* expression is seen in the ENCC (arrow).

Scale bar in **C-F**: 60 μM

Figure S8. **Annotated Atlas labeled by cell-types.**

(A) UMAP visualization of cells labeled by source identity (either 48-50 hpf or 68-70 hpf) following integration. All 48-50 hpf cells approximately map to a major cluster found at 68-70 hpf.

(B) Following label transfer integration, major cell type classifications group together into distinct clusters.

(C) High resolution visualization of both hierarchical clustering of cell categories as well as their position within the UMAP. Cell categories segregate in the dendrogram largely as expected from the UMAP visualization.

(D) Additional markers for validation of the Neural/Neuronal clusters.

Figure S9. **Resources for generation and preparation of whole mount chromogenic *in situ* and HCR probes.**

(A) Novel probes for *notch1a*, *dla*, and *foxc1a* were generated via PCR with the listed primers. Sources from previously published probes are also listed.

(B) Table of genes used for HCR analysis. HCR amplifier ID is listed to demonstrate capacity for multiplexing with probes such that each assay contains only unique IDS. All probes were designed by Molecular Instruments to target the named Refseq Transcriptome sequence as listed.

Table S1. Top significantly enriched genes per cluster in the *sox10*:GFP scRNA-seq data sets

Table S2. Top significantly enriched genes per sub-cluster, following subset and re-clustering of Cluster 5 and 12 at 68-70 hpf.

Table S3. Top significantly enriched genes per Major Cell Type identity in the *sox10*:GFP merged Atlas.

Table S4. Melanophore Populations shared and unique genes at 68-70 hpf.

FIGURE 1

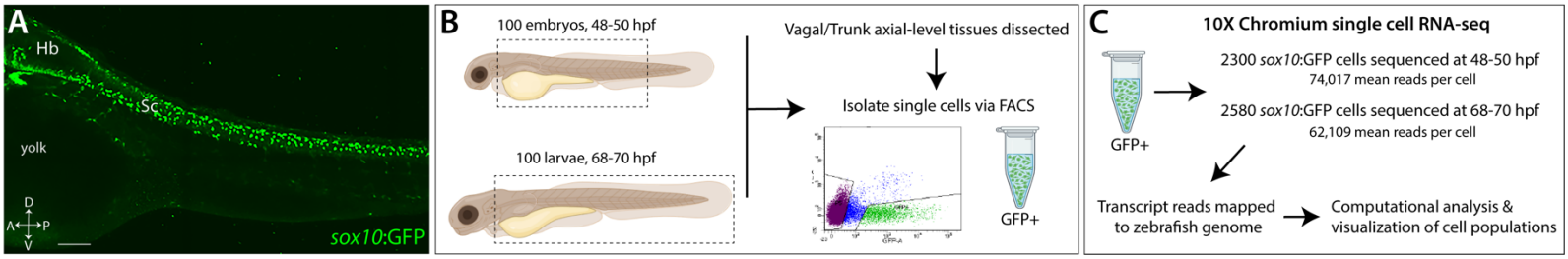

FIGURE 2

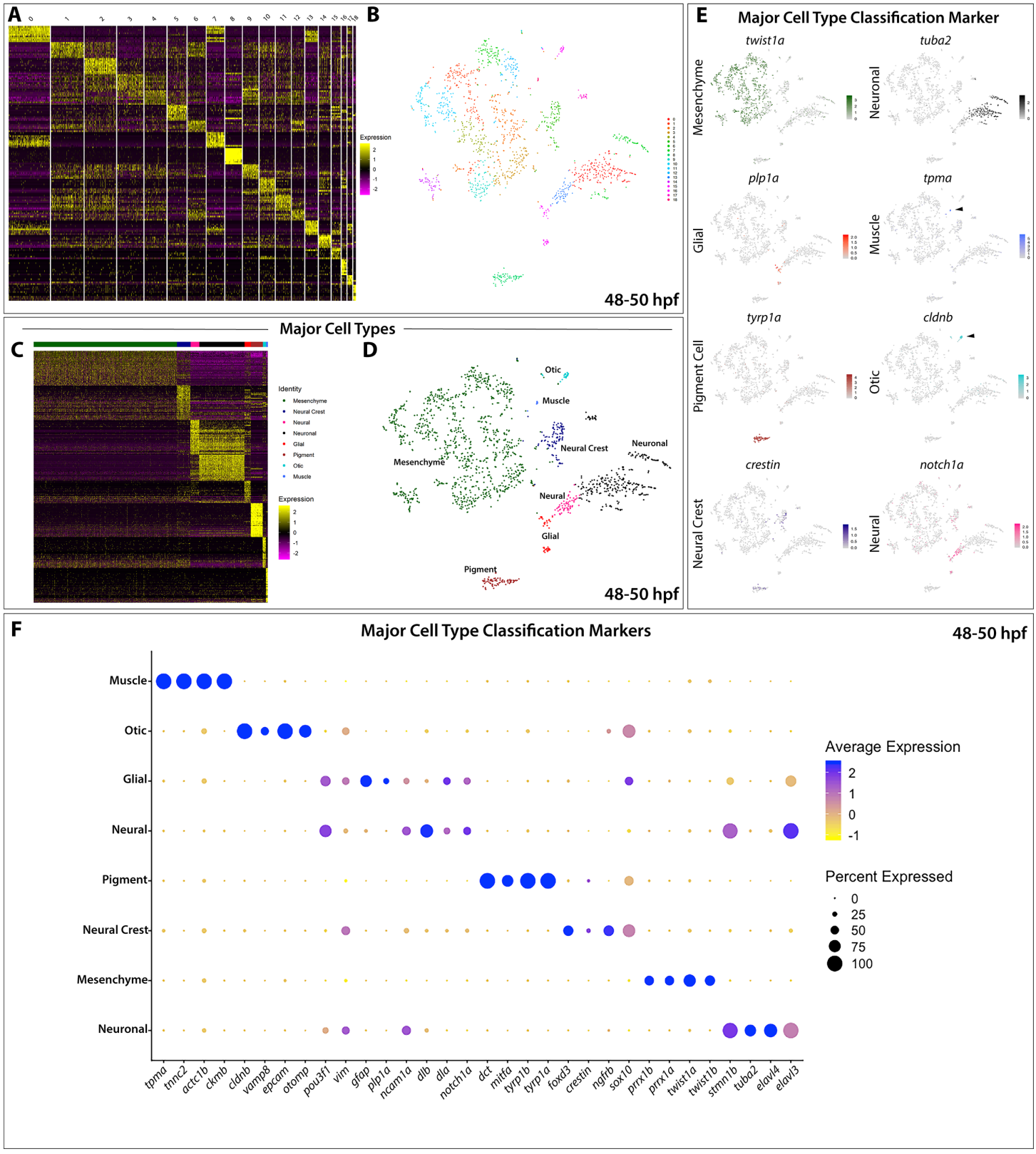

FIGURE 3

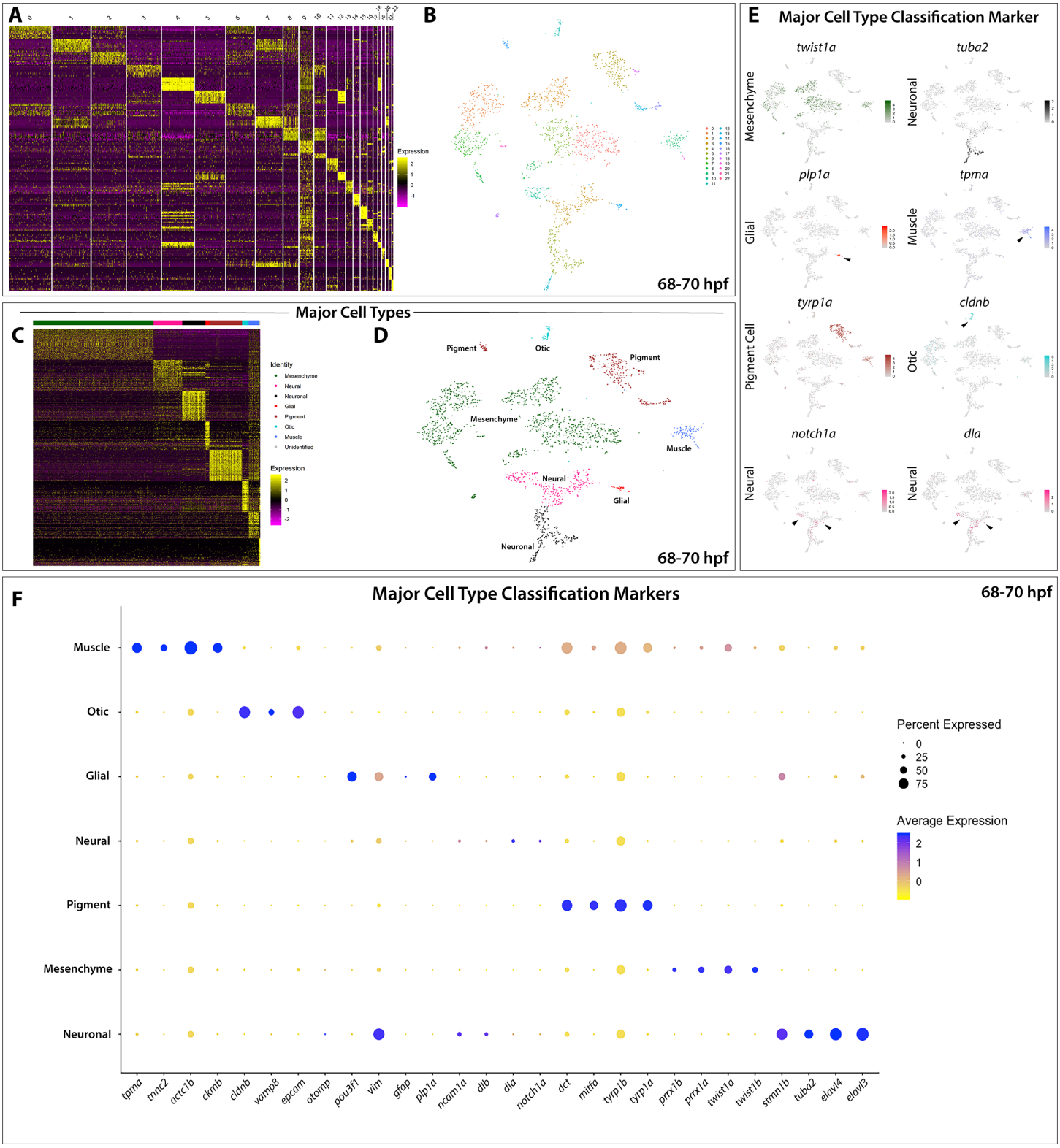

FIGURE 4

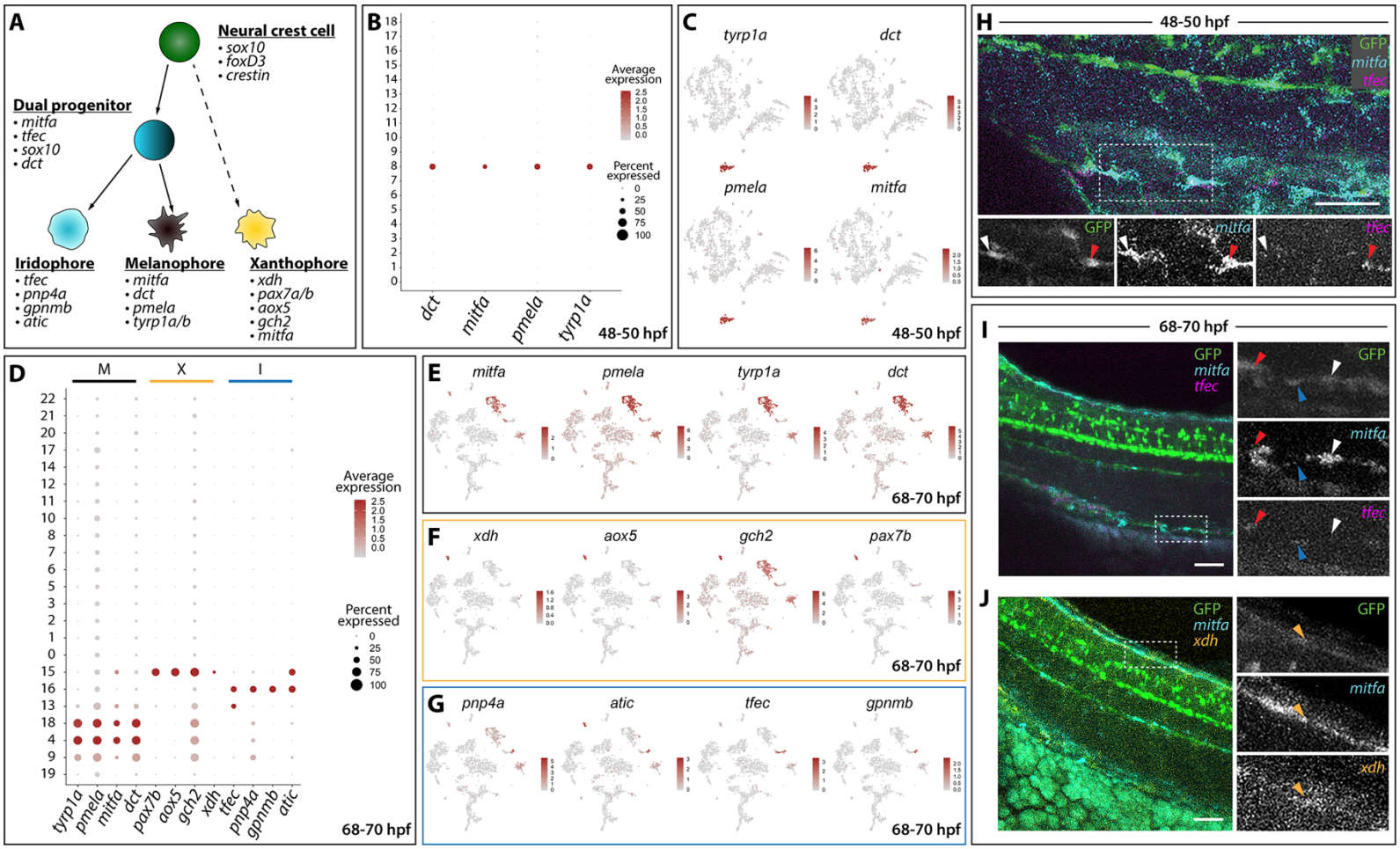

FIGURE 5

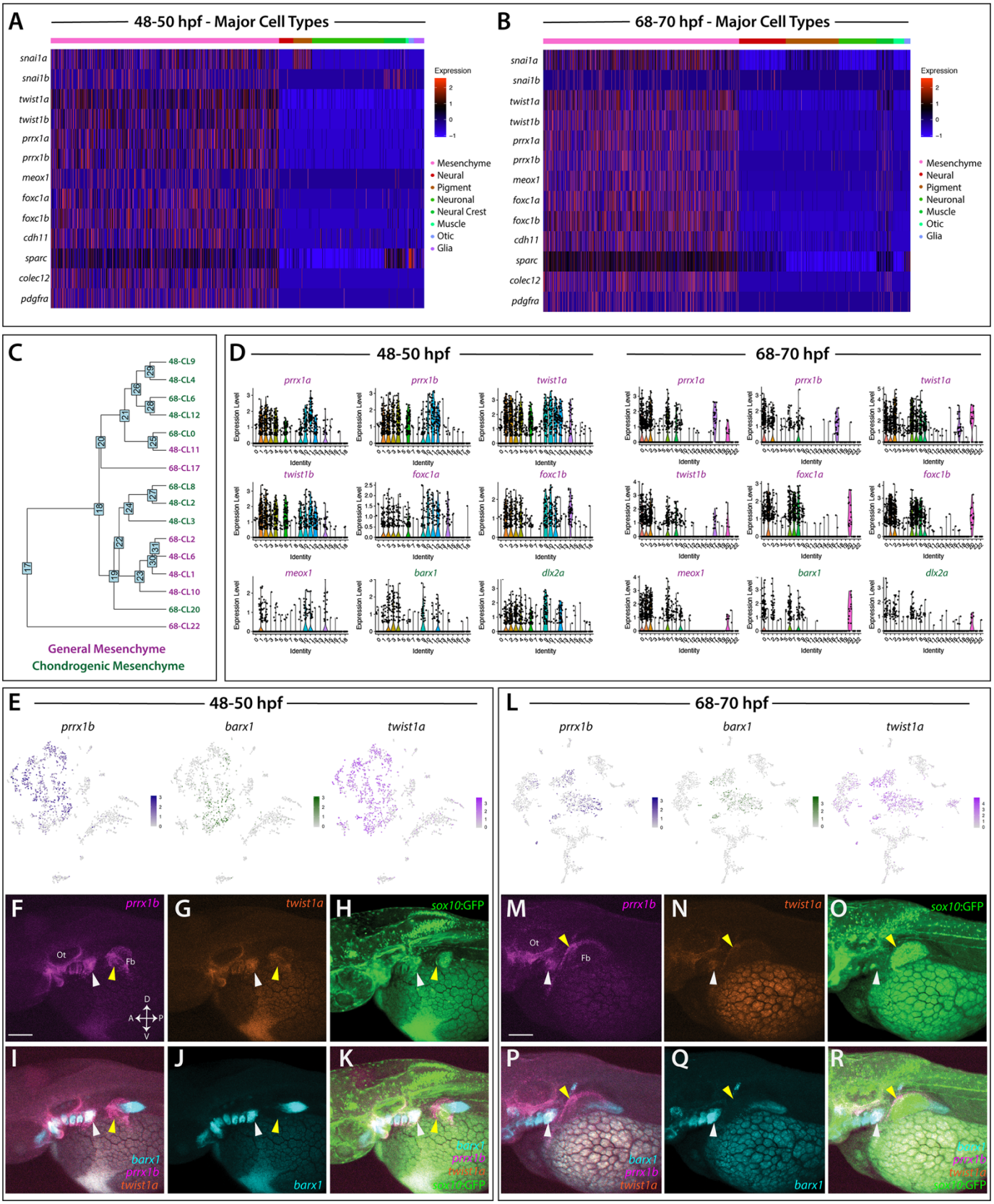

FIGURE 6

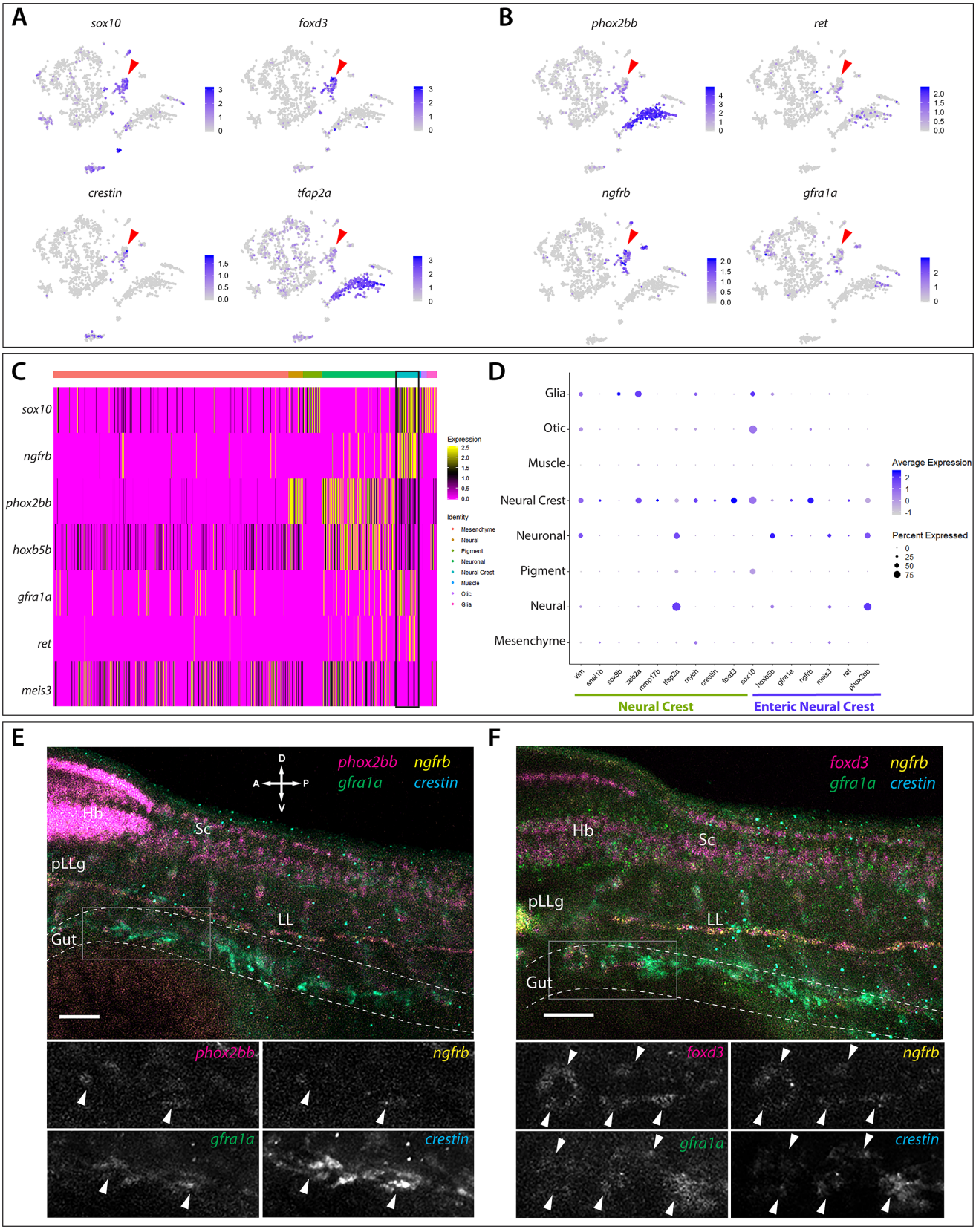

FIGURE 7

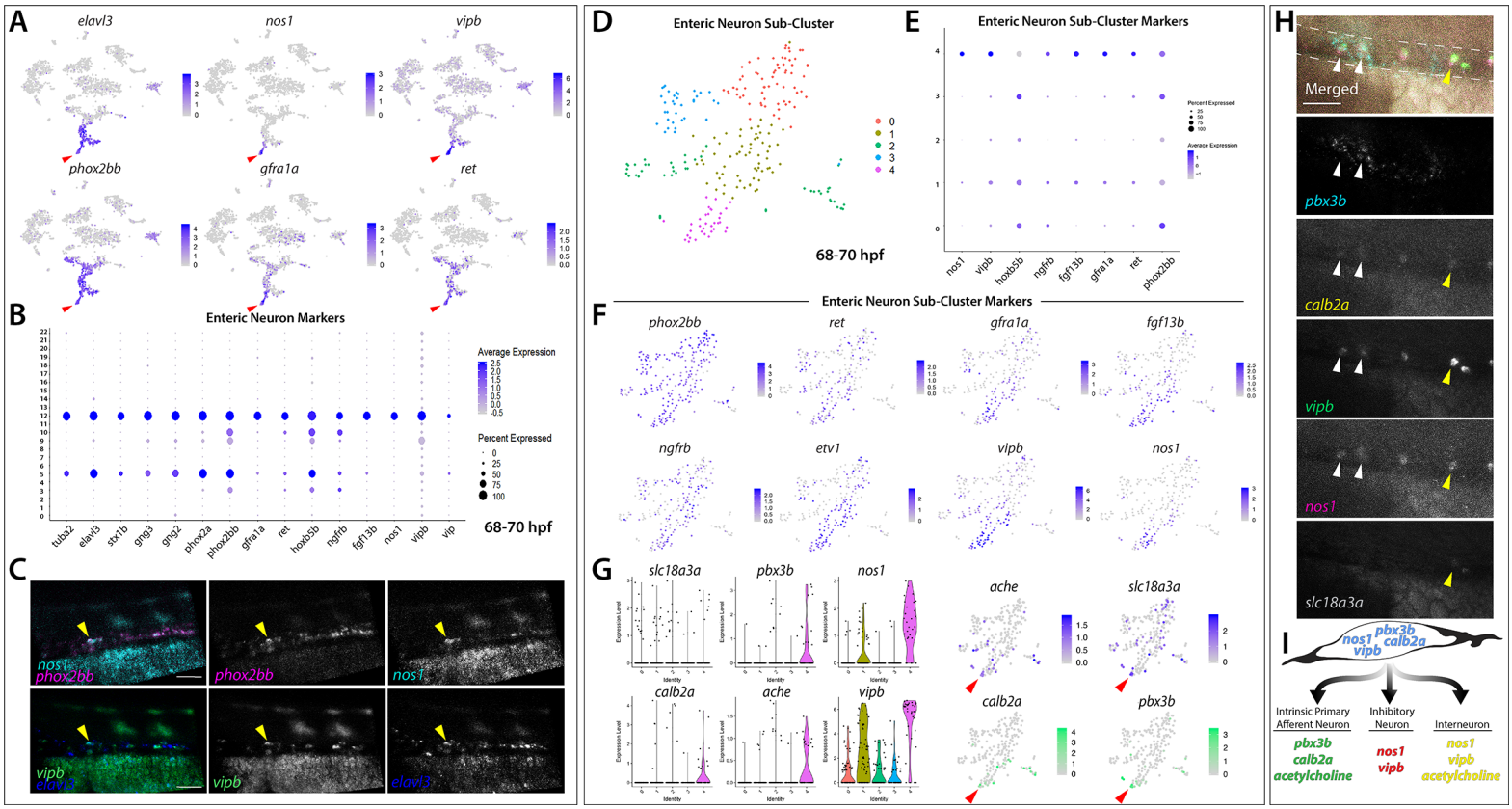

FIGURE 8

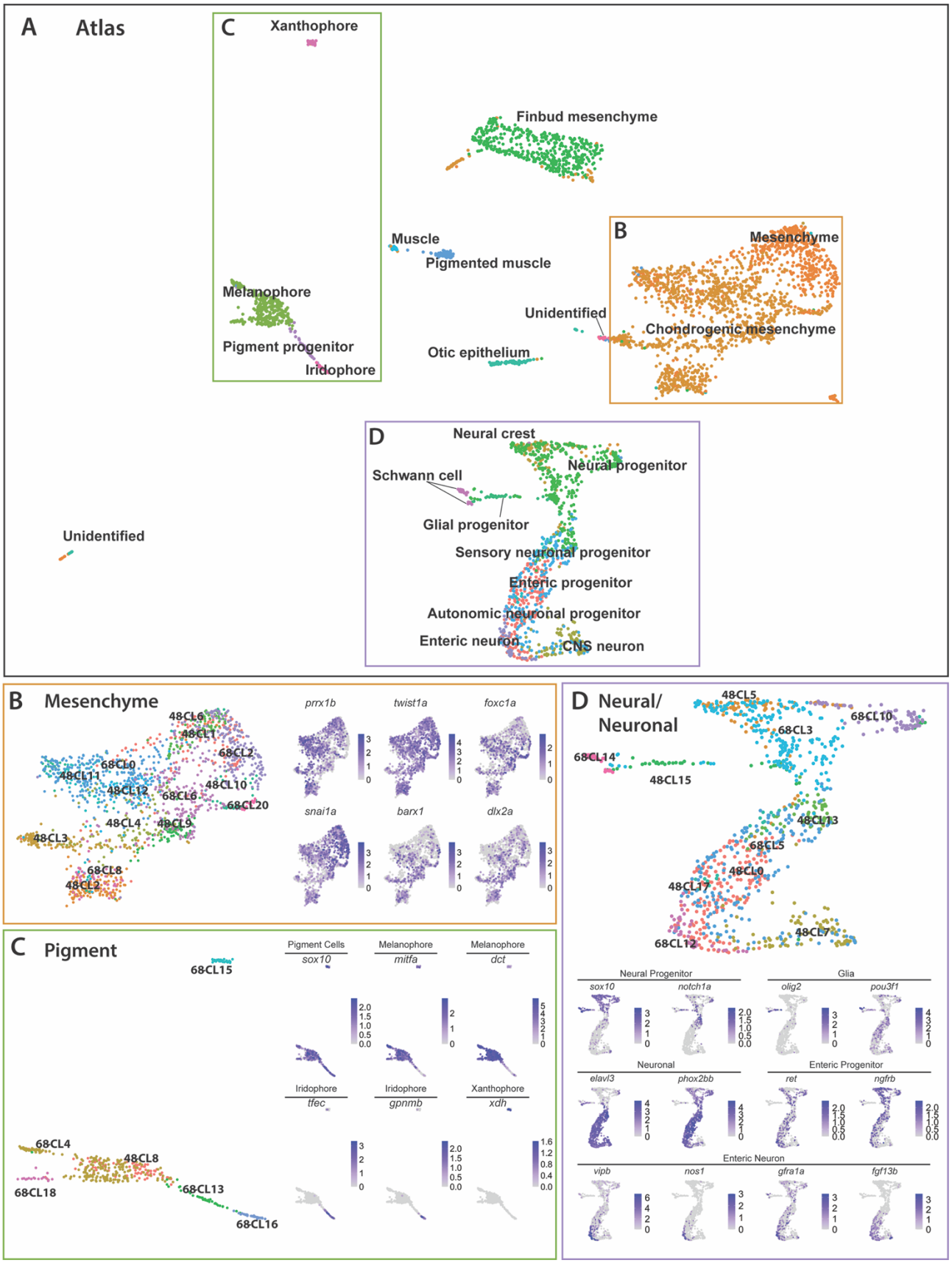

FIGURE 9

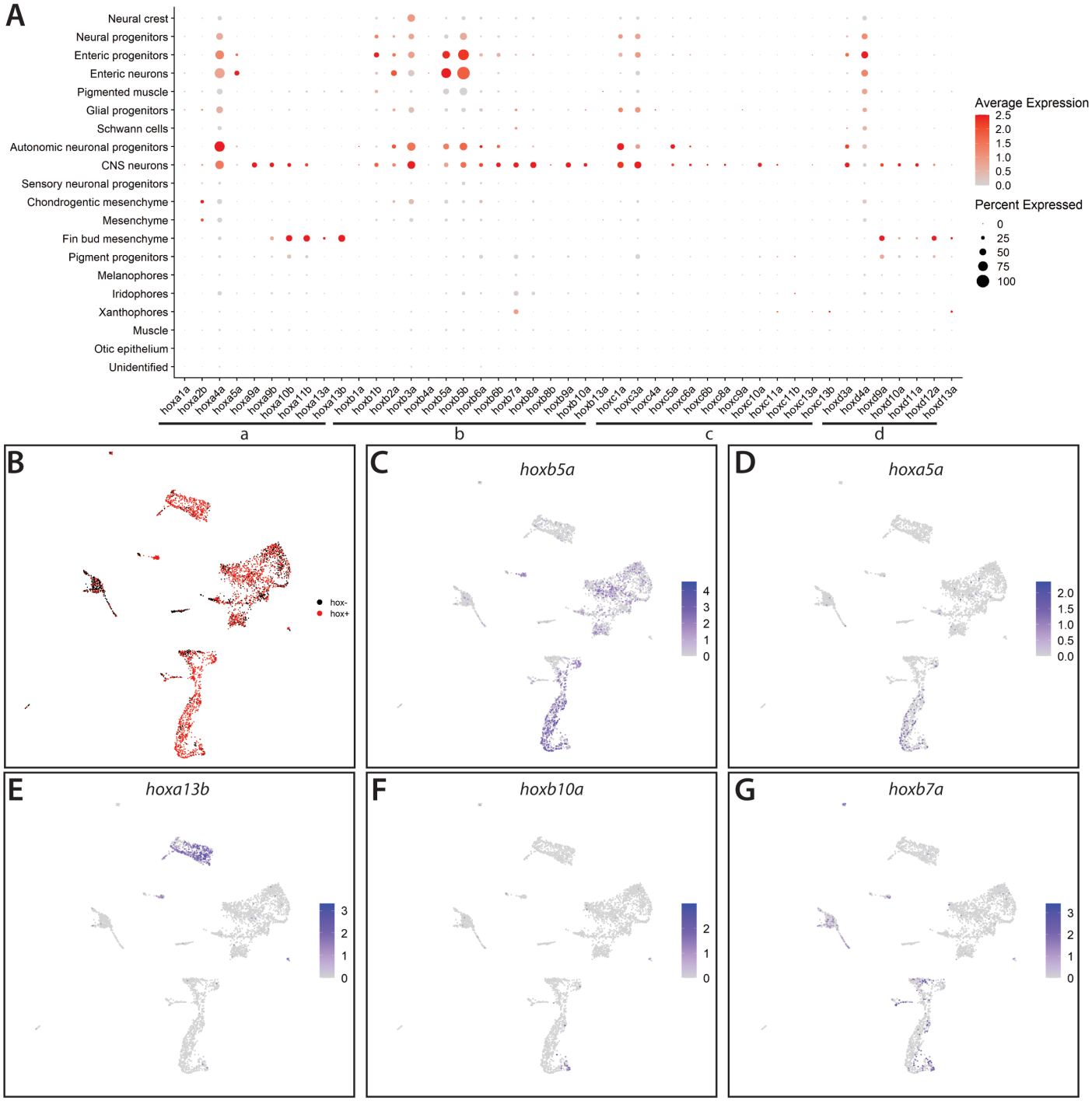

FIGURE S1

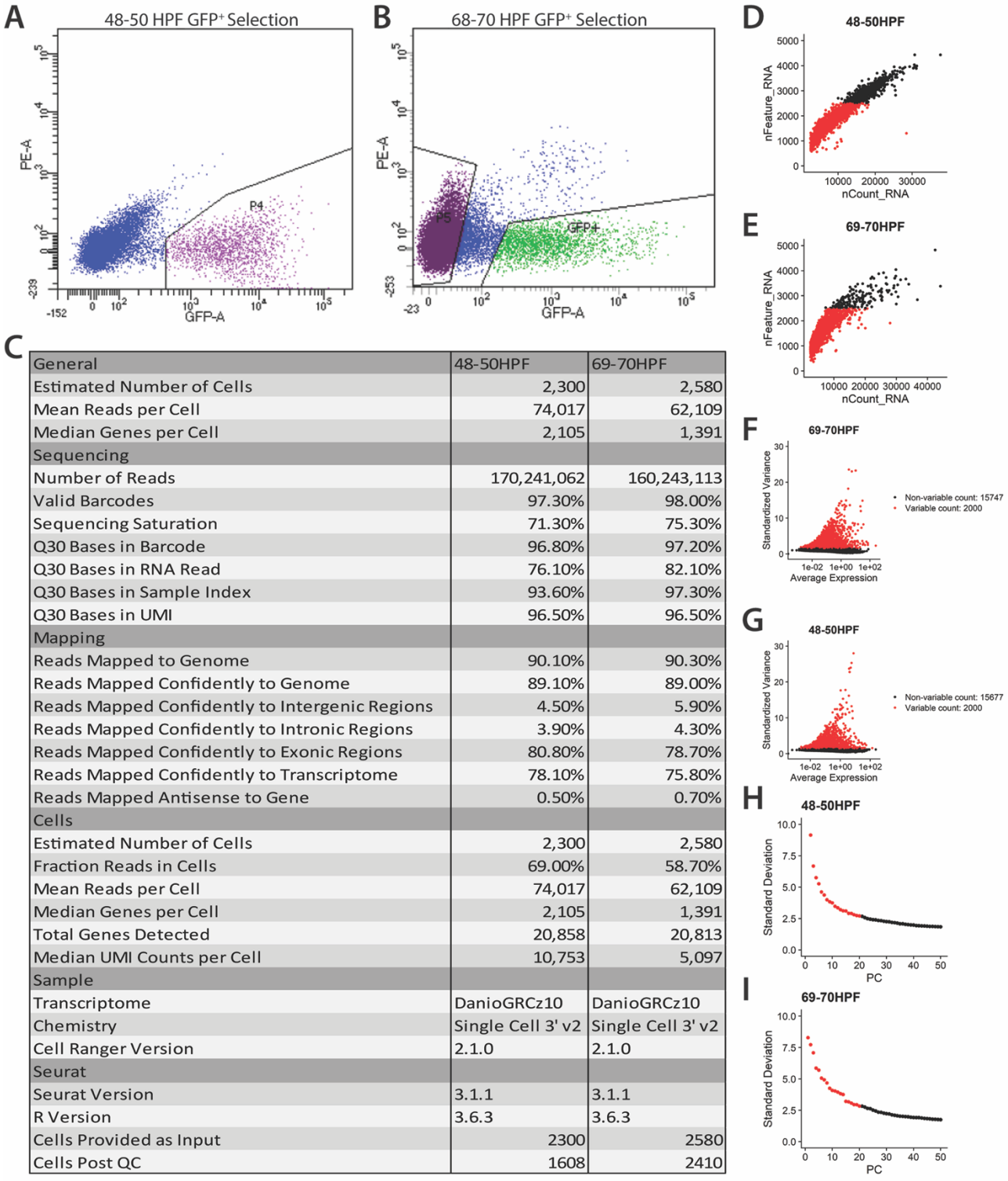

General	48-50HPF	69-70HPF
Estimated Number of Cells	2,300	2,580
Mean Reads per Cell	74,017	62,109
Median Genes per Cell	2,105	1,391
Sequencing		
Number of Reads	170,241,062	160,243,113
Valid Barcodes	97.30%	98.00%
Sequencing Saturation	71.30%	75.30%
Q30 Bases in Barcode	96.80%	97.20%
Q30 Bases in RNA Read	76.10%	82.10%
Q30 Bases in Sample Index	93.60%	97.30%
Q30 Bases in UMI	96.50%	96.50%
Mapping		
Reads Mapped to Genome	90.10%	90.30%
Reads Mapped Confidently to Genome	89.10%	89.00%
Reads Mapped Confidently to Intergenic Regions	4.50%	5.90%
Reads Mapped Confidently to Intronic Regions	3.90%	4.30%
Reads Mapped Confidently to Exonic Regions	80.80%	78.70%
Reads Mapped Confidently to Transcriptome	78.10%	75.80%
Reads Mapped Antisense to Gene	0.50%	0.70%
Cells		
Estimated Number of Cells	2,300	2,580
Fraction Reads in Cells	69.00%	58.70%
Mean Reads per Cell	74,017	62,109
Median Genes per Cell	2,105	1,391
Total Genes Detected	20,858	20,813
Median UMI Counts per Cell	10,753	5,097
Sample		
Transcriptome	DanioGRCz10	DanioGRCz10
Chemistry	Single Cell 3' v2	Single Cell 3' v2
Cell Ranger Version	2.1.0	2.1.0
Seurat		
Seurat Version	3.1.1	3.1.1
R Version	3.6.3	3.6.3
Cells Provided as Input	2300	2580
Cells Post QC	1608	2410

FIGURE S2

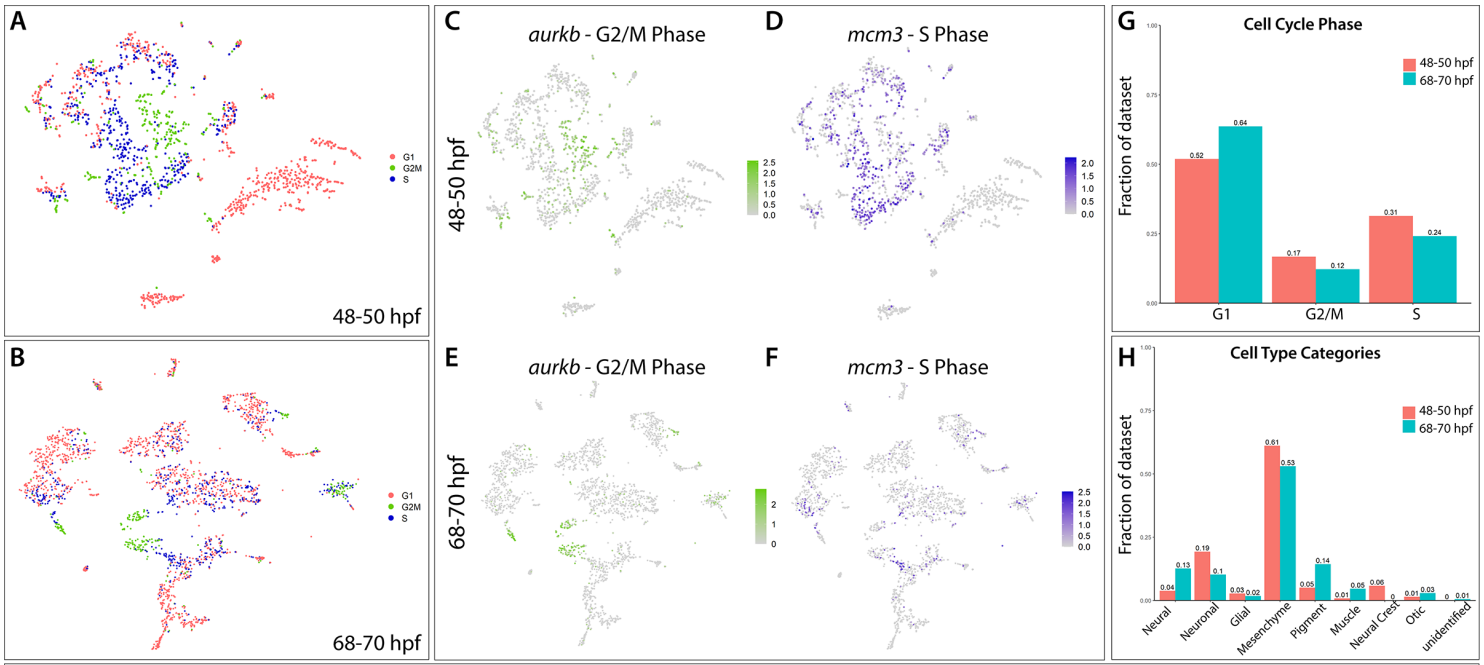

I

S Phase	*ccnd1*	*pcna*	*chaf1a*	*cdca7a*	*hells*	*gmnn*	*pold1*	*msh2*	*mcm4*	*mcm5*	*mcm6*	*fen1*	*mcm3*
G2/M Phase	*arhgef39*	*asf1ba*	*atad2*	*aurkb*	*birc5a*	*ccna2*	*ccnb1*	*ccnb2*	*ccnb3*	*cdca8*	*cdk1*	*cks1b*	*cks2*
	dck	*dlgap5*	*foxm1*	*g2e3*	*h2afx*	*hmmr*	*smc4*	*kiaa0101*	*kif11*	*knstrn*	*kpna2*	*ube2c*	*mad2l1*
	mibp	*mki67*	*neil3*	*ncapd2*	*prc1b*	*nusap1*	*plk1*	*rpa3*	*rrm2*	*rrm2.1*	*spc25*	*zgc:110540*	*ube2t*
	top2a	*tpx2*											

FIGURE S3

Time Point	Cluster ID #	Major Cell Type	Subtype	Identifier genes	# of Cells in Cluster	Citations
48-50HPF	cl0	Neuronal	Autonomic Neuronal Progenitor	**phox2bb**, **tfap2a/b**, **elavl3/4**, **phox2a**, tuba2, ncam1a, draxin,sncb,fez1,cdh2	201	Farnsworth et al., 2020; Soldatov et al., 2019
48-50HPF	cl1	Mesenchyme	Mesenchymal Progenitor	**prrx1a**, **snai1a**, **twist1a**, **foxc1b**, mcm5, pcna, mcm7,cdh11, meox1	160	Soldatov et al., 2019
48-50HPF	cl2	Mesenchyme	Chondrogenic Mesenchyme Proliferative 1	**dlx2a**, **prx1a/b**, **twist1a/b**, **barx1**, cdk1,ccna2	154	Soldatov et al., 2019; Sperber et al., 2008; Sperber and Dawid, 2008; Ding et al., 2013; Barske et al., 2016
48-50HPF	cl3	Mesenchyme	Chondrogenic Mesenchyme Proliferative 2	**barx1, dlx2a**, **mcm6**, **prrx1b**, chaf1a,pcna,hand2	129	Soldatov et al., 2019; Sperber et al., 2008; Sperber and Dawid, 2008; Ding et al., 2013; Barske et al., 2016
48-50HPF	cl4	Mesenchyme	Chondrogenic Mesenchyme Stem-like	**prrx1a**, **dlx2a**, **barx1**, **twist1a**, rpa1, fen1, rpa2, uhrf1, id3, chaf1a	108	Soldatov et al., 2019; Sperber et al., 2008; Sperber and Dawid, 2008; Ding et al., 2013; Barske et al., 2016
48-50HPF	cl5	Neural Crest	Migratory Neural Crest/ Enteric Neural Crest	**sox10**, **foxd3**, **crestin**,**tfap2a,** mmp17b, pcdh10a,phox2bb, ret, ngfrb, gfra1a,	93	Dutton et al., 2001; Luo et al., 2001; Knight et al., 2003; Stewart et. al., 2006
48-50HPF	cl6	Mesenchyme	Mesenchyme Differentiating 1	**foxc1a**, **twist1a, tagln2,aldh1a2,** rdh10a, meis3, cyp26a1, hand2, tpm4a, actb1	88	Soldatov et al., 2019
48-50HPF	cl7	Neuronal	Central Nervous System neuron	**gad1b,gad2, slc6a5,slc32a1,gata2a,**irx1b, elavl3, elavl4, tuba2, phox2bb	86	Farnsworth et al. 2020
48-50HPF	cl8	Pigment	Melanophore	**typr1a/b**, **mitfa**, **dct**, **pmela**, slc45a2, sox10, mlpha, tspan10, oca2	81	Du et al., 2003; Lister et al., 1999; Ludwig et al., 2004; Quigley and Parichy, 2002
48-50HPF	cl9	Mesenchyme	Chondrogenic Mesenchyme Migratory	**dlx2a, barx1**, **foxc1a**, **twist1a**, dlx4a, id2a, snai1a/b, twist3	77	Soldatov et al., 2019; Sperber et al., 2008; Sperber and Dawid, 2008; Ding et al., 2013; Barske et al., 2016
48-50HPF	cl10	Mesenchyme	Mesenchyme Differentiating 2	**cdh11**, **foxc1a/b, prrx1a, meox1**, pdgfra, col2a1a, col9a1a, col9a2, sparc, colec12, reck	74	Soldatov et al., 2019
48-50HPF	cl11	Mesenchyme	Mesenchymal Migratory	**cxcl12a, cxcl12b, rac1,reck**, foxc1a, twist1a, prrx1a, meox1, snai2	74	Soldatov et al., 2019
48-50HPF	cl12	Mesenchyme	Chondrogenic Mesenchyme Proliferative 3	**prrx1b**, **twist1b**, **foxc1a**, **barx1**, cyp26a1, rdh10a, meis3, aldh1a2, mcm5, mcm6	61	Soldatov et al., 2019
48-50HPF	cl13	Neural	Neural Progenitor	**notch1a**, **dla/b**, **olig4**, **elavl3**, phox2ba, neurod4, scrt2, phox2bb, ncam1a	61	Farnsworth et al., 2020
48-50HPF	cl14	Mesenchyme	Fin Bud	**tbx5a**, **hand2**, **hoxa13a/b, prrx1a/b,** foxc1b, hoxd13a, pcna	58	Yelon et al., 2000;Lu et al., 2019;Nakamura et al., 2016;Feregrino et al., 2019
48-50HPF	cl15	Glial	Peripherial Glial Progenitor	**sox10**, **olig1/2**, **fabp7a**, **notch1a**, sox3, nkx2.2a, pou3f1,plp1a,gfap,s100b	44	Soldatov et al., 2019; Carney et al. 2006
48-50HPF	cl16	Otic	Otic Epithelium	**sox10, cdh1, otomp,cldnb**, cldn7b, cldnh, epcam, aldh1a3,vamp8	23	Thisse et al., 2004; Thisse et al., 2005
48-50HPF	cl17	Neuronal	Sensory Neuronal Progenitor	**ngfrb**, **neurod1**, **neurod4**,**vim** neurog1, grfra1a, six1a/b, elavl4, isl2a/b, pou4f1	23	Soldatov et al., 2019
48-50HPF	cl18	Muscle	Muscle	**ckmb, actc1b, tnnc2, tnnt3a**, pvalb2, tnnt3b, ak1, tpma, desma	13	Thisse et al., 2004
68-70HPF	cl0	Mesenchyme	Chondrogenic Differentiating Mesenchyme 1	**barx1, sparc, prrx1a/b**, **twist1a/b**, pdgfra, col1a2, col6a1, col5a1	281	Soldatov et al., 2019; Sperber et al., 2008; Sperber and Dawid, 2008; Ding et al., 2013; Barske et al., 2016
68-70HPF	cl1	Mesenchyme	Fin Bud	**tbx5a, hand2,prrx1a/b , hoxd13a,** pcna, foxc1a/b, meox1,hoxa13a/b	254	Yelon et al., 2000;Lu et al., 2019;Nakamura et al., 2016;Feregrino et al., 2019
68-70HPF	cl2	Mesenchyme	Mesenchymal Migratory	**meox1**, **prrx1a**/b, **foxc1b**, snai1a, cdh11, rac1a, myl9b, **twist1a/b**	229	Soldatov et al., 2019
68-70HPF	cl3	Neural	Neural Progenitor	**fabp7a, foxd3**, **sox10, phox2bb**, her4.2, mdka, her4.1, ccnd2a, ngfrb, tuba8l	228	Farnsworth et al. 2020
68-70HPF	cl4	Pigment	Melanophore	**mitfa**, **pmela**, **tyrp1a**/b, **dct**, oca2, mlpha, tspan10, tfap2e	213	Du et al., 2003; Lister et al., 1999; Ludwig et al., 2004; Quigley and Parichy, 2002
68-70HPF	cl5	Neuronal	Sympatho-enteric Progenitor	**ascl1a, phox2bb**, **phox2a**, **hand2**, insm1a/b, dpysl3, ret, ngfrb, gfra1a,elavl3/4	202	Thisse et al., 2004;Heanue and Pachnis, 2008
68-70HPF	cl6	Mesenchyme	Chondrogenic Differentiating Mesenchyme 2	**barx1**, **prrx1a**, **foxc1a/b, twist1a**, col1a2, col5a1, cdh11, dlx5a, sparc,meox1	191	Soldatov et al., 2019
68-70HPF	cl7	Mesenchyme	Fin Bud	**tbx5a, hand2, hoxa13a/b,prrx1a/b** , hoxd13a, pcna, sox10	178	Yelon et al., 2000;Lu et al., 2019;Nakamura et al., 2016;Feregrino et al., 2019
68-70HPF	cl8	Mesenchyme	Chondrogenic Proliferative Mesenchyme	**prrx1a/b**, **foxc1a**, **twist1a/b**, **barx1**,col2a1a, pcna, cdc6, ccnb2	98	Soldatov et al., 2019
68-70HPF	cl9	Muscle	Pigmented Muscle	**tnnt3b, mitfa**, **tyrp1a**,**tpma**, ckmb, gch2, dct, tnnc2, myl1,	93	Thisse et al., 2004; Thisse et al., 2005
68-70HPF	cl10	Neural	Neural Progenitor	**sox10**, **foxd3, ascl1a, aurkb**, ncam1b, ccna2, tpx2, phox2bb, ret, elavl3/4	76	Farnsworth et al. 2020
68-70HPF	cl11	Otic	Otic Epithelium	**cldne**, **vamp8, cldnb**, **epcam**, cldn7b, cldnh, cdh1	70	Thisse et al., 2004, Thisse et al., 2001
68-70HPF	cl12	Neuronal	Enteric Neuron	**elavl3/4, phox2bb, gfra1a, ret,** fgf13b, vip, vipb, nos1, ngfrb, hoxb5b	44	Shepherd et al., 2004; Heanue and Pachnis, 2008; Uyttebroek et al., 2010; Taylor et al., 2016; Gaudet et al., 2011
68-70HPF	cl13	Pigment	Pigment Progenitor	**sox10**, **tfec**, **tfap2e, mitfa,** zeb2a, cdh1, mlpha, pax3a, trpm1b, gpx3	43	Saunders et al., 2019
68-70HPF	cl14	Glial	Schwann Cells	**sox10**, **mbpa/b, pou3f1, egr2b,** fabp7a, erbb3a, plp1a, cx27.5, gldn, mag	42	Farnsworth et al. 2020
68-70HPF	cl15	Pigment	Xanthophore	**xdh**, **pax7a/b**, **gch2, aox5**	39	Nord et al., 2016; Parichy et al., 2000; Saunders et al., 2019; Minchin and Hughes, 2008; Lister et al., 1999
68-70HPF	cl16	Pigment	Iridiophore	**atic, gpnmb, tfec, pnp4a**	32	Higdon et al., 2013; Lister et al., 2011; Petratou et al., 2018, 2019
68-70HPF	cl17	Mesenchyme	Differentiating Mesenchyme 1	**twist1a,prrx1a,colec12**, **sparc**, mmp2, msx2b, col5a1, col1a1a, pdgfra, tnc	25	Soldatov et al., 2019
68-70HPF	cl18	Pigment	Proliferative Melanophores	**mitfa, pmela, tyrp1a/b, aurkb,** pcna, cenph, mlpha, dct, ggr143, tfap2e	19	Du et al., 2003; Lister et al., 1999; Ludwig et al., 2004; Quigley and Parichy, 2002
68-70HPF	cl19	Muscle	Muscle	**ckmb, tpma, tnnc2, tnnt3b**, actc1b, cavin4a, myom1a, neb, flnca, desma,	18	Thisse et al., 2004
68-70HPF	cl20	Mesenchyme	Chondrogenic Mesenchyme Migratory	**barx1, twist1a**, **foxc1a/b, snai1a**, dlx3b, mmp2, sparc, snai2, dlx2a, sox9a	16	Soldatov et al., 2019
68-70HPF	cl21	Unidentified/Spurious	Unidentified/Spurious	anxa2b, cldnc, faah2b, vil1, fabp1b.1, plac8.1	13	
68-70HPF	cl22	Mesenchyme	Differentiating Mesenchyme 2	**rac2**, **sparc**, **col18a1**, **col2a1b,** col1a1a, lama5, thy1	6	Soldatov et al., 2019

FIGURE S4

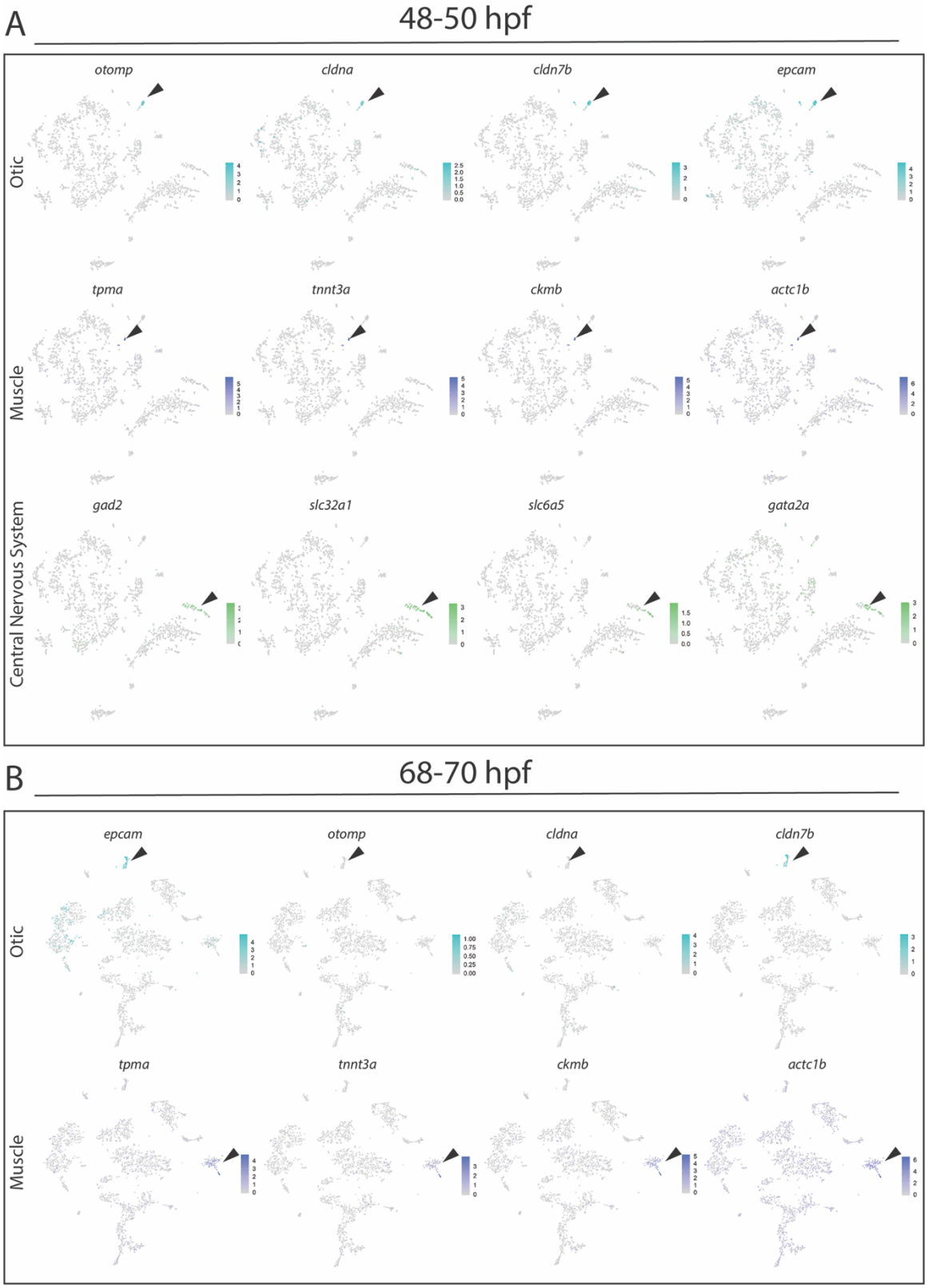

FIGURE S5

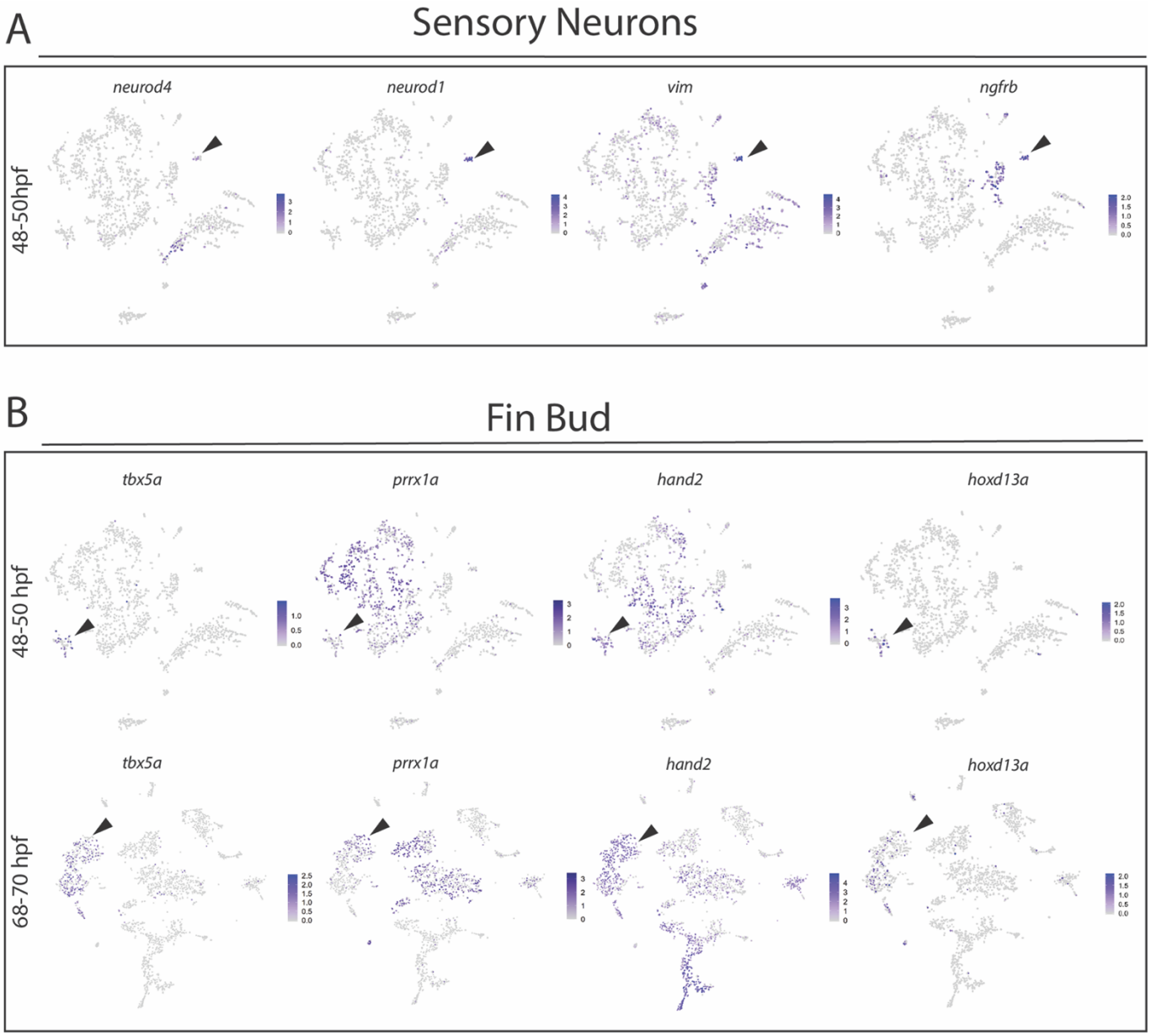

FIGURE S6

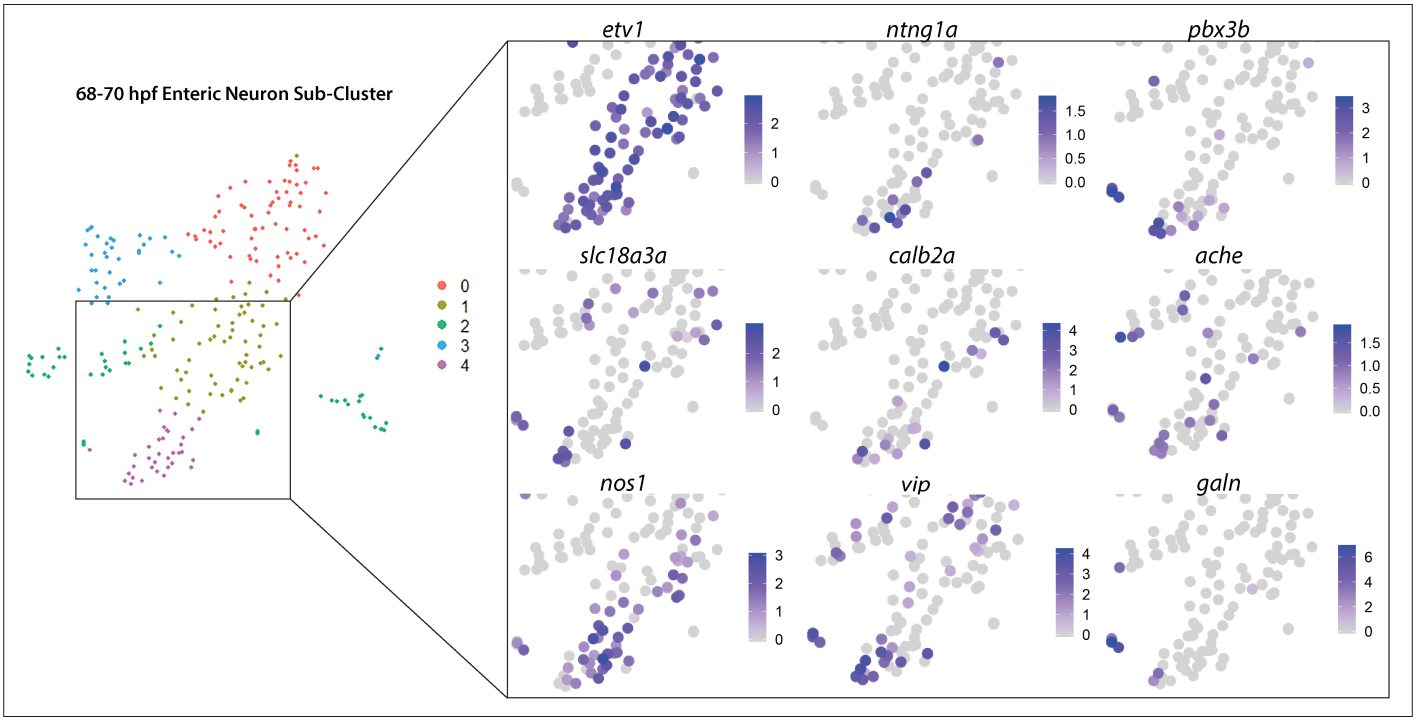

FIGURE S7

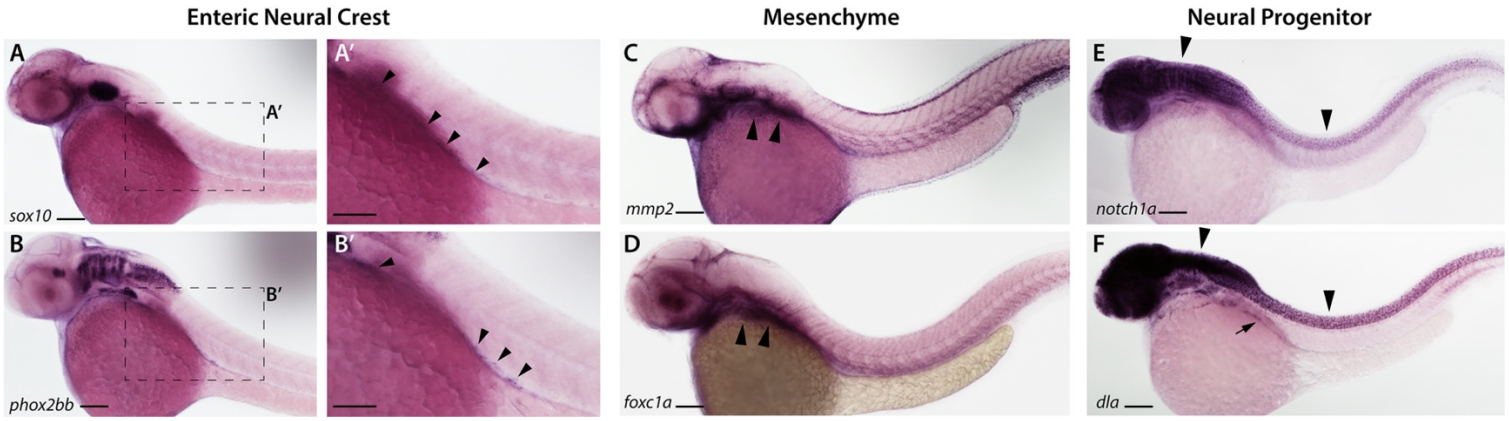

FIGURE S8

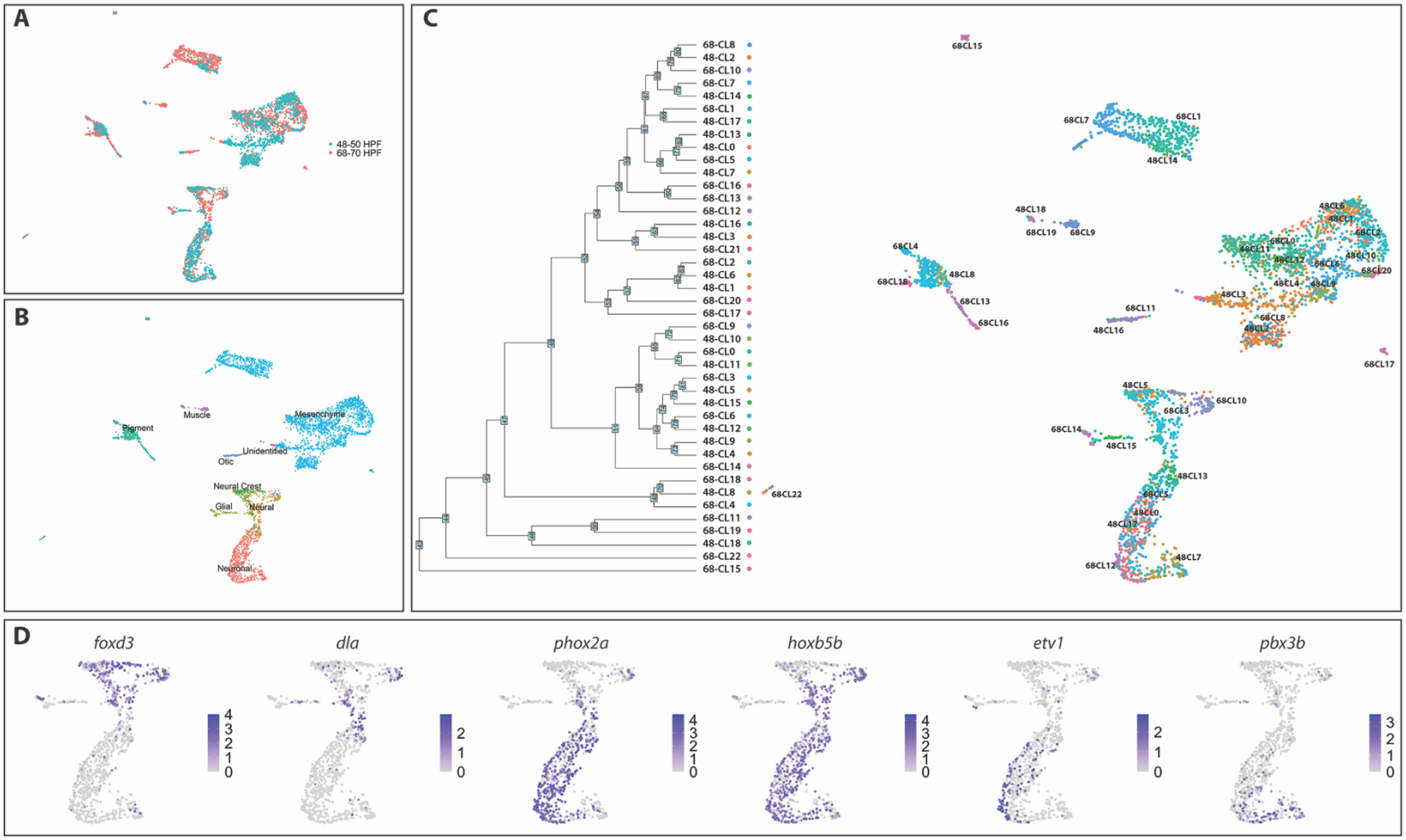

FIGURE S9

A

In Situ probes		
Gene	**Forward Primer**	**Reverse Primer**
notch1a	CAGTGGACTCAGCAGCATC	CCTTCCGACCAATCAGACAAG
dla	CAGCCAAGTTGCTCAGAG	GTACAGAGAACCAGCTCATC
foxc1a	ATACGGTGGACTCTGTGG	CAGCGTCTGTCAGTATCG

Gene	**Source**
phox2bb	Uribe and Bronner, 2015
sox10	Dutton et al., 2001
mmp2	Strausberg et al., 2002

B

Gene Name	HCR amplifier	Refseq Transcript ID	Gene Name	HCR amplifier	Refseq Transcript ID
barx1	B3	NM_001024949.1	*pbx3b*	B2	BC131865.1
calb2a	B1	NM_200718.1	*phox2bb*	B1	NM_001014818.1
crestin	B3	AF195881.1	*prrx1b*	B4	NM_200050.1
elavl3	B2	NM_131449	*slc18a3a*	B3	NM_0010775550.1
gfra1a	B4	NM_131730.1	*tfec*	B2	NM_001030105.2
mitfa	B1	NM_130923.2	*twist1a*	B1	NM_130984.2
ngfrb	B5	NM_001198660.1	*vipb*	B4	NM_001114555.1
nos1	B5	NM_131660.1	*xdh*	B5	XM_683891.7